UNIVERSIDAD NACIONAL AUTÓNOMA DE MÉXICO

PROGRAMA DE MAESTRÍA Y DOCTORADO EN INGENIERÍA

CENTRO DE INVESTIGACIÓN EN ENERGÍA

SIMULACIÓN NUMÉRICA DE LA DINÁMICA DE BURBUJAS EN DOS DIMENSIONES

TESIS

QUE PARA OBTENER EL GRADO DE

MAESTRO EN INGENIERÍA

ENERGÍA - FUENTES RENOVABLES DE ENERGÍA

PRESENTA:

SAÚL PIEDRA GONZÁLEZ

DIRECTOR DE TESIS:

DR. EDUARDO RAMOS MORA

2011

Universidad Nacional Autónoma de México
UNAM
Biblioteca Central
Dirección General de Bibliotecas de la UNAM

UNAM – Dirección General de Bibliotecas
Tesis Digitales
Restricciones de uso

DERECHOS RESERVADOS ©
PROHIBIDA SU REPRODUCCIÓN TOTAL O PARCIAL

Todo el material contenido en esta tesis esta protegido por la Ley Federal del Derecho de Autor (LFDA) de los Estados Unidos Mexicanos (México).

El uso de imágenes, fragmentos de videos, y demás material que sea objeto de protección de los derechos de autor, será exclusivamente para fines educativos e informativos y deberá citar la fuente donde la obtuvo mencionando el autor o autores. Cualquier uso distinto como el lucro, reproducción, edición o modificación, será perseguido y sancionado por el respectivo titular de los Derechos de Autor.

JURADO ASIGNADO:

Presidente: Dr. Mariano López de Haro

Secretario: Dr. Eduardo Ramos Mora

Vocal: Dr. Octavio Cazares Candia

1er. Suplente: Dr. Sergio Cuevas García

2do. Suplente: Dr. Luis Miguel De la Cruz Salas

Lugar donde se realizó la tesis:

Centro de Investigación en Energía, Temixco, Morelos, México.

TUTOR DE TESIS:

Dr. Eduardo Ramos Mora

FIRMA

Dedicado a:

A mi esposa Cinthya, por el gran amor y cariño que me ha dado.

A mi madre y toda mi familia por su apoyo incondicional.

A mis abuelos que aunque ya no están conmigo llenaron mi vida de felicidad.

Agradecimientos

A la Universidad Nacional Autónoma de México especialmente al Centro de Investigación en Energía por el apoyo brindado durante mis estudios de maestría.

A mis amigos que me apoyaron durante estos dos años de trabajo y le dieron un toque especial al tiempo que he estado en este Centro de Investigación, José Antonio, Joel, Manuel, Carlos, Michel, Gerardo, Aldo, Alberto y José de quien siempre recibí un gran apoyo para lograr los objetivos de este trabajo.

A los revisores, sus críticas y comentarios fueron de gran ayuda para mejorar la calidad de esta tesis.

A CONACyT (Consejo Nacional de Ciencia y Tecnología), por brindarme el financiamiento económico para realizar mis estudios de maestría.

Agradezco especialmente al Dr. Eduardo Ramos Mora por haberme permitido trabajar bajo su supervisión y apoyar mi desarrollo académico.

Contents

List of Figures

Resumen

En este trabajo se presenta un análsis numérico bidimensional de la dinámica de burbujas bajo diferentes condiciones de flujo. La tesis está enfocada a desarrollar herramientas numéricas para estudiar el flujo de burbujas ascendiendo en un fluido viscoso. Las simulaciones numéricas presentadas están basadas en los métodos de fronteras inmersas, particularmente usando el método de “front-tracking” para representar una interfase entre dos fluidos inmiscibles, encontrando las fuerzas interfaciales y calculando las propiedades materiales de cada fluido en todo el dominio. Esto permite resolver un solo conjunto de ecuaciones de conservación. Primeramente, se presenta la formulación matemática de los métodos de fronteras inmersas y su acoplamiento con las ecuaciones de Navier-Stokes. En el capítulo 2, se explica a detalle la estrategia numérica para implementar el método de “front-tracking” y la solución de las ecuaciones de Navier-Stokes. En la primera sección del capítulo 3, se reportan simulaciones numéricas del ascenso de una burbuja en una columna de fluido, para bajos y altos números de Reynolds. Para bajos números de Reynolds, las burbujas siguen una trayectoria lineal y su cauda es estable. Para altos números de Reynolds se encuentra un comportamiento más interesante donde las burbujas siguen una trayectoria en zig-zag aproximadamente periódica muy similar a la huella de vórtices de Von Kármán. En este punto se realizan comparaciones con un modelo fenomenológico y con observaciones experimentales realizadas en una celda Hele-Shaw. Estas comparaciones se hacen con el propósito de verificar las simulaciones numéricas. La última sección del capítulo 3 contiene los resultados de las simulaciones numéricas de la dinámica de varias burbujas. Uno de los fenómenos más importantes que se presenta cuando se estudian nubes de burbujas es la interacción de dos (o más) burbujas. Finalmente, diferentes arreglos de simulaciones para varias burbujas son brevemente presentados y analizados con el fin de ejemplificar algunas de las características de este tipo de sistemas.

Abstract

In this study, a two-dimensional numerical analysis of the dynamics of bubbles at different flow conditions is presented. This thesis is focused in the development of numerical tools to analyze in detail the flow of bubbles rising in a viscous fluid. The numerical simulations done are based on the immersed boundary methods for fluid interfaces, in particular using the front tracking method to represent an interface between two different immiscible fluids, calculating the interfacial forces and computing the material properties of the fluids in the entire integration domain. This is achieved by solving a single set of conservation equations. First, the mathematical formulation of the immersed boundary methods and the coupling with the Navier-Stokes equations are presented. In Chapter 2, the numerical strategy to implement the front tracking method and the solution of the Navier-Stokes equations are explained in detail. In the first sections of Chapter 3, the numerical simulations of a single bubble rising in a column of fluid are reported, both, for low and high Reynolds numbers. At low Reynolds numbers, the bubbles follow a straight path and the wake is steady. A more interesting behavior is found at high Reynolds numbers where the bubbles follow an approximately periodic zig-zag trajectory and an unstable wake with properties similar to the Von Kármán vortex street is formed. The comparison of the numerical results with a phenomenological model and Hele-Shaw cell experiments is also presented in this chapter with the purpose of verifying the numerical simulations. In the final section of Chapter 3 we present the numerical results of simulations of multiple bubbles. One of the fundamental effects when bubble clouds are studied is the interaction of two bubbles. This is explored in this thesis in an effort to understand the complex dynamics involved on it, in particular in the zones of strong interactions. Finally, the different arrays of multiple bubbles are briefly presented and analyzed. The behavior of this kind of systems is intricate and the calculations presented are given as an illustration of some aspects of the complex dynamics.

Introduction

Multi-fluid systems are of fundamental importance in many natural processes and in a host of industrial activities such as combustion, chemical reaction, petroleum refining and boiling. The rising of a single bubble in a viscous liquid due to buoyancy is one of typical multi-fluid systems. However, a comprehensive knowledge of the flow behavior and mechanism of such multi-fluid systems in full flow regimes is still lacking, although a number of experimental, theoretical analysis and numerical studies have addressed this problem. The first recorded observation of the rise of bubbles is to be found in the writings of Leonardo da Vinci. About five centuries ago, Da Vinci summarized his observations on the motion of air bubbles in a liquid in the following manner:

> *The air that submerged itself with the water which percussed upon the other water, returns to the air, penetrating the water in sinuous movement, changing its substance into a great number of forms. And this happens because the light thing cannot remain under the heavy; rather it is continuously pressed by the part of the liquid which rests upon it; and because the water that stands there perpendicular is more powerful than the other in its decent, this water is always driven away by the part of the water that form its coverings, and so moves more continually sideways where it is less heavy and in consequence offers less resistance, according to the 5th [proposition] of the 2nd [book]; and because this "has to make its movement by the shortest way", it never spreads itself out from its path except the extent which it avoids the water which covers it above.*

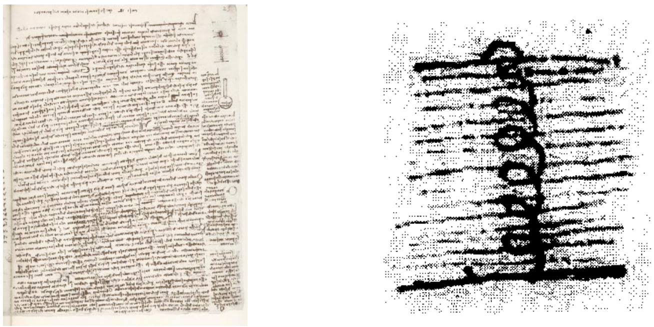

Figure 1: Leonardo's manuscript known as Codex Leicester. The small sketch in the right-hand side shows the spiraling motion of a rising bubble.

Leonardo da Vinci's words are beautifully expressed in the picture of Figure 1 which is contained in the Codex Leicester. Many experimental works have reported several results about the behavior of a single rising bubble, (Bhaga & Weber 1981) and (Sanada, Shirota & Watanabe 2007) are some examples. On the other hand, approximate theoretical solutions have been derived in the limit of very small bubble deformations for either high or low Reynolds numbers, where the bubble shape is relatively stable. Bubble shapes, trajectories and terminal velocities of the bubbles for different flow conditions have been reported in the experimental works, a complete range of shapes of bubbles can be found in (Clift, Grace & Weber 1978). It is commonly observed that bubbles rise in axi-asymmetric trajectories, straight, spiral or zigzag. However, the mechanisms of these motions of bubbles are not yet fully understood and thus remain as an open question (Mougin & Magnaudet 2002). The understanding on bubble rise and deformation is still limited to a few flow regimes only, due to the difficulties in experiments. It is rather difficult to measure, without any interference, the flow pattern and pressure distribution within a bubble and its surrounding liquid while it is rising and deforming.

Considering the difficulties in experimental and theoretical investigations, numerical simulations provide an effective alternative approach to attain a better insight into the bubble rising behavior, the development of bubble shape evolution and the flow behavior in the viscous liquid. In recent years, significant progress has been made in understanding and modeling bubbles rising in a column of fluid by advanced numerical simulations, particularly, using the immersed boundary methods (Hua & Lou 2007), (Ohta, Imura, Yoshida & Sussman 2005), (Chen, Garimella, Reizes & Leonardi 1999). In contrast with the average models (e.g. two-fluids models), the immersed boundary methods provide detailed information about the interface of the fluids; in these methods, the conservation equations are solved without any modeling assumptions. The most popular methods based on this formulation are the volume of fluid, level set, marker particle, shock capturing and front tracking, to name a few. The numerical simulations of bubbles using the volume of fluid method have been widely used to try to understand the behavior of bubbles at different flow conditions, see for instance (Krishna & van Baten 1999) and (Scardovelli & Zaleski 1999). However, many problems are presented when this method is implemented, the most critical problem is that artificial coalescence or rupture of bubbles can occur (van Sint Annaland, Deen & Kuipers 2005). Another approach used to simulate multiphase flows is the level set method (see (Sussman, Smereka & Osher 1994) and (Sussman, Fatemi, Smereka & Osher 1998) for details). The implementation of this method is very simple in two and three dimensions but its accuracy is limited and artificial coalescence and break up of the bubbles also occur. The front-tracking method is another alternative to compute multi-fluid systems as the rising of bubbles (Unverdi & Tryggvason 1992), (Hua & Lou 2007), (Gunsing 2004). This method is extremely accurate because the interface is tracked explicitly using marker points connected to each other. Then, artificial coalescence does not occur due to the fact that a separate mesh is used to track the interface, but this method is difficult to implement since the interface of the fluids requires a remeshing algorithm each time step.

In the present thesis, a two dimensional numerical study of the rising of bubbles in a column of fluid is presented. The implementation is based on the solution of the Navier-Stokes equations coupled with a front-tracking method. Numerical simulations of a single bubble are presented in two parts, the first is devoted to the analysis of the motion of bubbles at low Reynolds number, and a detailed study of the rising of bubbles at this flow conditions is presented. The shape of the bubbles, terminal velocities and external flows are calculated. In the second part, the bubbles rising at high Reynolds are studied, the features of the oscillatory motion of the bubble and the unstable wake are explored. At these flow conditions a phenomenological model proposed by (Pesavento & Wang Jane 2004) is adapted to compute the rising of a single bubble. The simulations of the front-tracking model are then compared with the results of the phenomenological model, and the forces identified in the phenomenological model are analyzed separately to describe the effect of each of them over the bubble. Also, to complete the study of a single bubble, the results of the numerical simulations are compared with experiments in a Hele-Shaw cell. This is an interesting physical situation that approximates the motion of bubbles in two dimensions, i.e. this problem can be regarded as the two dimensional case of freely moving bubbles. This phenomenon has been described by (Kelley & Wu 2005), see also (Ramos, Sanchez, Gonzalez & Herrera 2007). The last part of the present investigation focuses on the interaction of multiple bubbles rising in a viscous fluid. First, the interactions of two bubbles are studied. Then effect of the vortices detached by the first bubble over the path of the second bubble is analyzed. Further, the interaction of multiple bubbles rising simultaneously are computed, and a brief study of this phenomenon is given. However, the extreme complexity of the dynamical interactions between multiple bubbles prevents us to offer a complete understanding of the physics involved in this problem.

Chapter 1

Mathematical Formulation

In this chapter, the governing equations of two immiscible fluids are presented using the one fluid approach with local density and viscosity variation to take into account the separate phases. We restrict the analysis to a two phase flow, for which the front tracking method has been widely used. This method can be classified as an immersed boundary that combines the capabilities of the level set and volume of fluid methods. The material properties of the two different fluids are calculated using an indicator function obtained from the position of the interface of the fluids.

1.1 The immersed boundary methods

There are several ways to simulate multiphase flows; some classical examples are averaged models, boundary integral and Lattice Boltzmann methods. Other alternatives include immersed boundary methods for fluid interfaces. Commonly the immersed boundary methods are applied to simulate systems in which elastic structures interact with fluid flows (Peskin 1977), however it is possible to extend this theory to the cases where fluid interfaces exist. The immersed boundary methods for multiphase flows have been widely applied in many different systems and various methods based on that formulation such as volume of fluid, level set and the front tracking methods are available.

The mark-and-cell method can be conceived as the oldest version of the immersed boundary methods in which marker particles are used to identify each phase. Specifically, this method was used by researchers at the Los Alamos National Laboratory in the early 1960s and permitted the first successful simulation of the finite Reynolds number motion of free surfaces and fluid interfaces. On the other hand, in the volume of fluid method, a marker function is used to find the interface between the two fluids (Scardovelli & Zaleski 1999). This function is advected using the velocity field found when the momentum equations are solved in the domain. The level set is a widely used method, where a marker function is used to identify the different fluids in the domain and no assumption is made on the connectivity of the interface. This method allows an accurate computation of two phase flows including topological changes in the interface, like break up or coalescence of bubbles (Sussman et al. 1994), however, in flow fields with appreciable vorticity or in cases where the interface is significantly deformed, level set methods suffer from loss of mass (volume) and hence loss of accuracy (van Sint Annaland et al. 2005). The front tracking method avoids solving an equation for a marker function, but the interface between the fluids must be tagged using an unstructured mesh with connected marker points that are advected with the flow and then the surface tension and the material properties are computed from the new location of the interface (Prosperetti & Tryggvason 2007).

In the present study, a two dimensional front tracking model that can be efficiently used to perform numerous computational experiments was implemented. The front tracking method was chosen because of its excellent capability to calculate the surface tension forces, which significantly effects in the bubble shape and dynamics. Other methods, like the classical volume of fluid, level set and mark-and-cell models, do not allow for such an accurate and detailed representation of the surface tension forces. A disadvantage of the front tracking method is, however, that the volume of the bubble is not intrinsically exactly conserved. The gas volume of the bubble slowly changes in time, caused by the method used to move the interface, the applied filters and the remeshing of the interface mesh. The markers that span the surface elements are moved with their local velocities. These local marker velocities are interpolated from the velocity field on the Cartesian grid. These interpolated velocities introduce minor small-scale anisotropy (Gunsing 2004). However, using a finer computational grid this problem can effectively be suppressed.

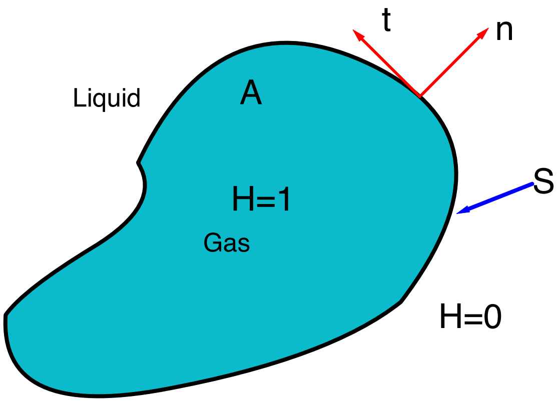

Figure 1.1: One fluid approach illustration in two dimensions.

In the immersed boundary methods it is possible to solve a single set of conservation equations using the “one fluid approach”. When a multiphase system is being analyzed, it is necessary to take into account the differences between the material properties of the fluids and the forces concentrated in the interface as the surface tension force. These forces can be represented as delta functions in the interface, and a Heaviside function is used in order to identify the different fluids in the domain [1] (Prosperetti & Tryggvason 2007).

---

[1] The various fluids can be identified by a step (Heaviside) function H, which is 1 where one particular fluid is and 0 elsewhere (Tryggvason, Bunner, Esmaeeli, Juric, Al-Rawahi, Tauber, Han, Nas & Jan 2001).

The Heaviside function H can be expressed in terms of an integral over the product of one-dimensional δ functions:

$$H = \int_A \delta(x - x')\delta(y - y')da', \tag{1.1}$$

where the integral is over an area A bounded by a contour S. From the integral is evident that the Heaviside function is one if the point (x,y) is enclosed by S and zero elsewhere (see Figure 1.1). The gradient of H is calculated for the primed variables of equation Eq. (1.1) or for the umprimed variables as follows:

$$\begin{aligned}\nabla H &= \int_A \nabla \left[\delta(x - x')\delta(y - y')\right] da' \\ &= -\int_A \nabla' \left[\delta(x - x')\delta(y - y')\right] da'.\end{aligned} \tag{1.2}$$

The integral over an area, can be transformed to a line integral using the following variant of the divergence theorem for gradients (Tryggvason et al. 2001) :

$$\nabla H = -\oint_S \left[\delta(x - x')\delta(y - y')\right] \mathbf{n}' ds'. \tag{1.3}$$

Since we know that S is a closed contour, most of the integral is zero and we can replace it by one over a part of the contour and drop the circle on the integral:

$$\nabla H = -\int_S \left[\delta(x - x')\delta(y - y')\right] \mathbf{n}' ds'. \tag{1.4}$$

If the material properties of each phase are considered constant, then a property in the entire domain, including the jump in the interface, can be written as:

$$\phi = \phi_1 H(x, y) + \phi_0(1 - H(x, y)), \tag{1.5}$$

where ϕ_1 is the property of the fluid in which $H = 1$ and ϕ_0 is the property of the fluid in which $H = 0$. The gradient of the property is:

$$\nabla\phi = \phi_1 \nabla H - \phi_0 \nabla H = (\phi_0 - \phi_1) \int_S \delta(x - x')\delta(y - y')\mathbf{n}' ds' \tag{1.6}$$

This mathematical formulation allows one to find the gradients of different material properties of the fluids in the whole domain. The conservation equations can then be solved in the domain even when fluids with different physical properties are present.

1.2 Conservation equations for two phase flow

The physical situation of interest in the present study is the motion of bubbles in a viscous fluid, and the model described is an idealization of that phenomenon. We consider a two dimensional complex fluid composed by a liquid and gas bubbles immersed in it. The equations that govern the momentum balance of the fluids are the Navier-Stokes equations:

$$\begin{aligned}\frac{\partial \rho \mathbf{u}}{\partial t} + \nabla \cdot \rho \mathbf{u}\mathbf{u} = -\nabla p + \nabla \cdot \mu (\nabla \mathbf{u} + \nabla^T \mathbf{u}) \\ + \int \sigma \kappa' \mathbf{n}' \delta^\beta (\mathbf{x} - \mathbf{x}') ds' + (\rho - \rho_f)\mathbf{g}\end{aligned} \tag{1.7}$$

The pressure is denoted by p, μ is the viscosity, $\mathbf{g}$ is the gravity vector, ρ_f is the density of the continuous phase, σ is surface tension and k' is curvature. The presence of the interface is incorporated by the term $\delta^\beta(\mathbf{x} - \mathbf{x}') = \delta(x - x')\delta(y - y')$, where $\mathbf{x}$ is the point at which the equations are evaluated and $\mathbf{x}'$ is a point in the interface. Formally, the integral is over the entire front, thereby adding the delta functions together to create a force that is concentrated at the interface, but smooth along the interface. It is important to note that this equation is valid for the whole field even when the density ρ and viscosity μ fields change discontinuously.

The mass conservation equation is given by:

$$\frac{\partial \rho}{\partial t} + \nabla \cdot \rho \mathbf{u} = 0 \tag{1.8}$$

For a single-phase flow where the density is constant, there is no need to follow the motion of individual fluid particles. However, if the density varies from one particle to another, but remains constant for each particle as it moves (as it must do for an incompressible flow), it is necessary to follow the motion of each fluid particle. This can be done by integrating the equation:

$$\frac{D\rho}{Dt} = 0 \tag{1.9}$$

For multiphase flows with well-defined interfaces where the density of each phase is a constant, we only need to find H and then construct the density directly from H as it was discussed in the section above. The same arguments hold for the viscosity and other properties of the fluid. The assumption given in Eq. (1.9) reduces the mass conservation equation to:

$$\nabla \cdot \mathbf{u} = 0 \tag{1.10}$$

The "one-fluid" equations are an exact rewrite of the Navier-Stokes equations for the fluid in each phase and the interface boundary conditions. The governing equations as listed above assume that the only complication in multifluid flows is the presence of a moving phase boundary with a constant surface tension.

1.3 Surface tension force

One of the most important elements in the immersed boundary methods implementation is the surface tension force calculation. This property depends of the curvature of the interface, and since the interface is deformed during the simulation, the curvature must be calculated in every time step.

For interfaces identified by connected marker points as is the case of the front tracking method, the computation of surface tension is, at least in principle, relatively straightforward. In most cases it is the total force on a small section of the front that is needed. In two dimensions we are generally working with a line element connecting two points and in three dimensions it is the force on a surface element connecting three points what is needed. Thus, the challenge is to find

$$\delta F_\sigma = \int_{\Delta s} \sigma \kappa \mathbf{n} ds \tag{1.11}$$

For a two-dimensional flow, we use the definition of the curvature of a plane:

$$\kappa \mathbf{n} = \frac{\partial \mathbf{t}}{\partial s} \tag{1.12}$$

where $\mathbf{t}$ is the unit tangent vector in the element of the front. Using equation (1.12) we can rewrite equation (1.11) as:

$$\delta F_\sigma = \sigma \int_{\Delta s} \frac{\partial \mathbf{t}}{\partial s} ds = \sigma(\mathbf{t}_2 - \mathbf{t}_1) \tag{1.13}$$

Therefore, instead of calculating the curvature, it is only required to find the tangents of the end points of each element of the interface. The simplest approach is to fit a parabola to the interface points and differentiate to obtain the tangent vectors. For higher accuracy, a polynomial is fitted through more points, and differentiated to give the tangent vector. In the present implementation, a cubic polynomial is fitted and four points are needed to be taken into account to calculate the tangent vectors of the endpoints of the front.

Chapter 2

Numerical Implementation

In this chapter, the numerical strategies to solve the Navier-Stokes equations and to implement the front-tracking method are explained. The finite volume method and the decoupling algorithm of the velocity and pressure are presented in the first section. The second part of the chapter is devoted to explain the steps to construct the front-tracking algorithm, the structure and tracking of the front are treated, also the technique to smooth and interpolate the front properties to the grid are presented.

2.1 Discretization of the Navier-Stokes Equations

The coupled momentum and mass conservation equations presented in Chapter 1, equations (1.7) and (1.10), must be discretized to render them in a suitable form to be numerically solved. Several strategies have been devised to accomplish this task and most of them have been described the literature. See for instance (M. Griebel & Neunhoeffer 1998) or (Versteeg & Malalasekera 1995). Note that although the mass and momentum equations must be simultaneously solved, the mass conservation equation does not involve the pressure. The solution algorithm must then involve some sort of decoupling. Again, many strategies have been proposed. Here we will describe somewhat in detail two of them, the projection scheme and the SIMPLE algorithm since they have been used in the present analysis. As it will be apparent in the conclusion of this document, the second algorithm gives better results.

The first-order projection method integrates the set of equations in two steps. The first part is a prediction step where the effect of the pressure is ignored as follows:

$$\frac{\rho^{n+1}\mathbf{u}^* - \rho^n\mathbf{u}^n}{\Delta t} = -\nabla\cdot\rho^n\mathbf{u}^n\mathbf{u}^n + \nabla\cdot\mu^n(\nabla\mathbf{u}^n + \nabla^T\mathbf{u}^n) + \mathbf{F}_\sigma + \mathbf{F}_{buoyancy}. \tag{2.1}$$

The second part is a correction step in which the pressure term is included,

$$\frac{\rho^{n+1}\mathbf{u}^{n+1} - \rho^n\mathbf{u}^*}{\Delta t} = -\nabla p. \tag{2.2}$$

The pressure is then calculated in such a way that the velocity in the new time step satisfies the mass conservation equation,

$$\nabla\cdot\mathbf{u}^{n+1} = 0. \tag{2.3}$$

Replacing Eq.(2.3) in Eq.(2.2) the pressure can be calculated with the expression,

$$\nabla \frac{1}{\rho^{n+1}} \cdot \nabla p = \frac{1}{\Delta t} \nabla \cdot \mathbf{u}^* \tag{2.4}$$

A special treatment is required for solving the pressure equation since the density is not a constant in the vicinity of the interface. In the early works that introduced the front-tracking method, a simple successive over relaxation (SOR) method was used, the results of the projection scheme were not satisfactory in the cases where the material properties of the fluids were very different, like for instance air and water, because the solution of the pressure equation diverges.

In order to avoid these difficulties, Hua et al. (Hua & Lou 2007) proposed that the coupling between flow velocity and pressure is solved by integrating the mass and momentum equations using the SIMPLE scheme. These authors report that their strategy may handle large density and viscosity ratios with accuracy.

Given that we are interested in comparing the results of our simulations with experimental observations of air bubbles in water, in this work, we followed the methodology described by (Tryggvason et al. 2001) for the front-tracking method, but the SIMPLEC method was used to solve the Navier-Stokes equations. We found that the simulation process is robust even in case of large density ratio because of the semi-implicit solving approach of the SIMPLEC sheme.The SIMPLEC algorithm was originally put forward by (Patankar. 1980) and is essentially a guess-and-correct procedure for the calculation of the pressure.

The momentum equations (Eq.1.7) are discretized in a regular staggered grid (see Figure 2.1) using the finite volume method as follows:

$$\frac{\mathbf{u}^{n+1} - \mathbf{u}^n}{\Delta t} = -\mathbf{u}^n \cdot \nabla \mathbf{u}^{n+1} + \frac{1}{\rho^{n+1}} \left(\nabla \cdot \mu^{n+1} (\nabla \mathbf{u}^{n+1} + \nabla^T \mathbf{u}^{n+1}) + \mathbf{F}_\sigma + \mathbf{F}_{buoyancy} \right) \tag{2.5}$$

In this implementation a hybrid scheme is used in the advection terms and central differences are used to discretize the pressure and diffusion terms. The discrete form of the conservation equations can be written as:

$$a_P u_P = \sum a_{nb} u_{nb} + S_P + S_e (p_P - p_E) \tag{2.6}$$

$$a_P v_P = \sum a_{nb} v_{nb} + S_P + S_n (p_P - p_N) \tag{2.7}$$

In two dimensions:

$$\sum a_{nb} u_{nb} = a_E u_E + a_W u_W + a_N u_N + a_S u_S \tag{2.8}$$

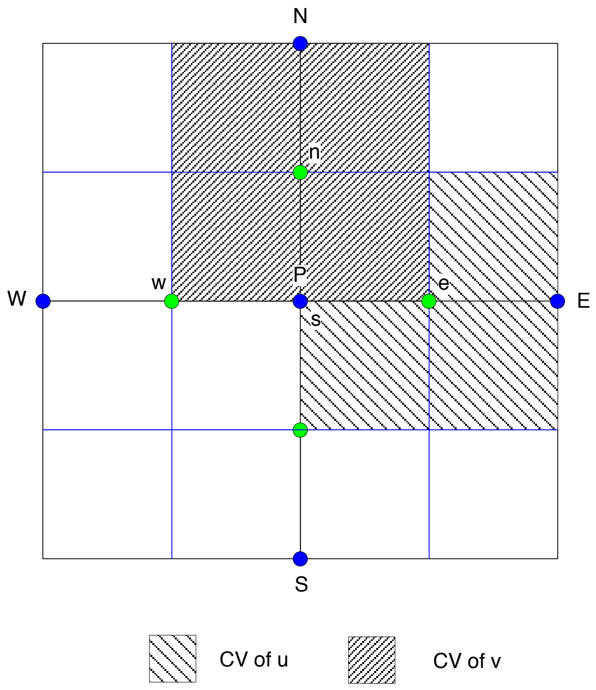

Figure 2.1: Staggered grid array.

From the staggered grid array the coefficients are calculated for the momentum conservation in the x direction as follows:

$$a_E = \frac{2\mu_{i+1,j} S_e}{\Delta x} - \frac{u_e S_e}{2} \tag{2.9}$$

$$a_W = \frac{2\mu_{i,j} S_w}{\Delta x} + \frac{u_w S_w}{2} \tag{2.10}$$

$$a_N = \frac{1}{4}\frac{(\mu_{i,j} + \mu_{i+1,j} + \mu_{i+1,j+1} + \mu_{i,j+1}) S_n}{\Delta y} - \frac{u_n S_n}{2} \tag{2.11}$$

$$a_S = \frac{1}{4}\frac{(\mu_{i,j} + \mu_{i+1,j} + \mu_{i+1,j-1} + \mu_{i,j-1}) S_s}{\Delta y} + \frac{u_s S_s}{2} \tag{2.12}$$

$$a_P = a_W + a_E + a_S + a_N + \frac{\Delta V}{\Delta t} \tag{2.13}$$

$$s_P = u^n_{i,j}\frac{\Delta V}{\Delta t} + 2\frac{(p_{i,j} - p_{i+1,j})\Delta y + F_{\sigma x}\Delta V + D_n + D_s}{\rho_{i+1,j} + \rho_{i,j}} \tag{2.14}$$

where

$$D_n = \frac{1}{4}\frac{(\mu_{i,j} + \mu_{i+1,j} + \mu_{i+1,j+1} + \mu_{i,j+1}) S_n}{\Delta x}(v^n_{i+1,j} - v^n_{i,j}) \tag{2.15}$$

$$D_s = -\frac{1}{4}\frac{(\mu_{i,j} + \mu_{i+1,j} + \mu_{i+1,j-1} + \mu_{i,j-1}) S_s}{\Delta x}(v^n_{i+1,j-1} - v^n_{i,j-1}) \tag{2.16}$$

And the coefficients for the momentum conservation in y direction are calculated as:

$$a_E = \frac{1}{4}\frac{(\mu_{i,j} + \mu_{i+1,j} + \mu_{i+1,j+1} + \mu_{i,j+1})S_e}{\Delta x} - \frac{u_e S_e}{2} \tag{2.17}$$

$$a_W = \frac{1}{4}\frac{(\mu_{i,j} + \mu_{i,j+1} + \mu_{i-1,j+1} + \mu_{i-1,j})S_w}{\Delta x} + \frac{u_w S_w}{2} \tag{2.18}$$

$$a_N = \frac{2\mu_{i,j+1} S_n}{\Delta y} - \frac{u_n S_n}{2} \tag{2.19}$$

$$a_S = \frac{2\mu_{i,j} S_s}{\Delta y} + \frac{u_s S_s}{2} \tag{2.20}$$

$$a_P = a_W + a_E + a_S + a_N + \frac{\Delta V}{\Delta t} \tag{2.21}$$

$$s_P = v^n_{i,j}\frac{\Delta V}{\Delta t} + 2\frac{(p_{i,j} - p_{i,j+1})\Delta x + F_{\sigma y}\Delta V + (0.5(\rho_{i,j+1} + \rho_{i,j})) - \rho_f)g_y + D_e + D_w}{\rho_{i,j+1} + \rho_{i,j}} \tag{2.22}$$

where

$$D_e = \frac{1}{4}\frac{(\mu_{i,j} + \mu_{i+1,j} + \mu_{i+1,j+1} + \mu_{i,j+1})S_e}{\Delta y}(u^n_{i,j+1} - u^n_{i,j}) \tag{2.23}$$

$$D_w = -\frac{1}{4}\frac{(\mu_{i,j} + \mu_{i,j+1} + \mu_{i-1,j+1} + \mu_{i-1,j})S_w}{\Delta y}(u^n_{i-1,j+1} - u^n_{i-1,j}) \tag{2.24}$$

To initiate the SIMPLEC calculation process a pressure field p^* is guessed. Discretized momentum Eqs. (2.6) and (2.7) are solved using the guessed pressure field to yield velocity components u^* and v^*.

$$a_P u^*_P = \sum a_{nb} u^*_{nb} + S_P + S_e(p_P - p_E) \tag{2.25}$$

$$a_P v^*_P = \sum a_{nb} v^*_{nb} + S_P + S_n(p_P - p_N) \tag{2.26}$$

Now we define the correction p' as the difference between the correct pressure field p and the guessed pressure field p^*, so that:

$$p = p^* + p' \tag{2.27}$$

In the same way, we define the velocity corrections u' and v' to relate the correct velocities to the guessed velocities u^* and v^*:

$$u = u^* + u' \tag{2.28}$$

$$v = v^* + v' \tag{2.29}$$

Subtracting the equations (2.25) and (2.26) from the equations (2.6) and (2.7), respectively:

$$a_P u'_P = \sum a_{nb} u'_{nb} + S_e(p'_P - p'_E) \tag{2.30}$$

$$a_P v'_P = \sum a_{nb} v'_{nb} + S_n(p'_P - p'_N) \tag{2.31}$$

In order to simplify equations (2.30) and (2.31) and following the SIMPLEC steps, it is necessary to subtract $\sum a_{nb} u'_P$ and $\sum a_{nb} v'_P$, on both sides of the equations. The equations can then be written as:

$$(a_P - \sum a_{nb}) u'_P = \sum a_{nb}(u'_{nb} - u'_p) + S_e(p'_P - p'_E) \tag{2.32}$$

$$(a_P - \sum a_{nb}) v'_P = \sum a_{nb}(v'_{nb} - v'_p) + S_n(p'_P - p'_N) \tag{2.33}$$

The term $(u'_{nb} - u'_p)$ should approximate zero as the grid size gets smaller, the first term on the right side of the equations (2.32) and (2.33) is neglected and the velocity correction is written as:

$$u'_P = d_u(p'_P - p'_E) \tag{2.34}$$

$$v'_P = d_v(p'_P - p'_N) \tag{2.35}$$

where:

$$d_u = \frac{S_e}{a_P - \sum a_{nb}} \tag{2.36}$$

$$d_v = \frac{S_n}{a_P - \sum a_{nb}} \tag{2.37}$$

Finally, an equation for the pressure correction is necessary to complete the system of equations. This is obtained by substituting equations (2.28) and (2.29) in the mass conservation equation:

$$a_P p'_P = \sum a_{nb} p'_{nb} + S_P \tag{2.38}$$

The definition of the coefficients for equation (2.38) are calculated as follows (De la Cruz 2005):

$$\begin{array}{ll} a_E = d_u S_e, & a_W = d_u S_w \\ a_N = d_v S_n, & a_S = d_v S_s \end{array} \tag{2.39}$$

$$S_P = -(u_e^* - u_w^*)\Delta y - (u_n^* - u_s^*)\Delta x \tag{2.40}$$

The source term in the pressure correction equation is the discrete form of the mass conservation equation (Eq. (2.40), when this source term is equal to zero, the velocities calculated satisfied the incompressibility condition and the SIMPLEC method converges.

2.2 Front-tracking method

2.2.1 Structure of the front, locating the front on the fixed grid

Given that the present study is restricted to two dimensions, the discussion in the present section will also be given in two dimensions. The front tracking method implementation requires a regular two dimensional grid and the tracked front that consists of points that are connected by elements (Figure 2.2). For each point, the only information stored is its coordinates. The elements are the lines that join two adjacent points and contain most of the front information. Each element is defined by the points that it is connected to, as well as the local structure of the front, including its neighboring elements.

The front is moved by the interpolation from the velocity field in the regular grid to each front point, and the surface tension force is calculated in the front points and interpolated to the regular grid to compute the conservation equations. The interpolation between the front and the regular grid will be discussed later.

To transfer information from the front to the uniform grid, we identify the point on the fixed grid that is closest to a given front position. In a one-dimensional case, if we denote the total number of grid points as NX and the total length of the domain as L_x, then the grid point to the left of a point at x is given by:

$$i = int(x \cdot NX/L_x) \tag{2.41}$$

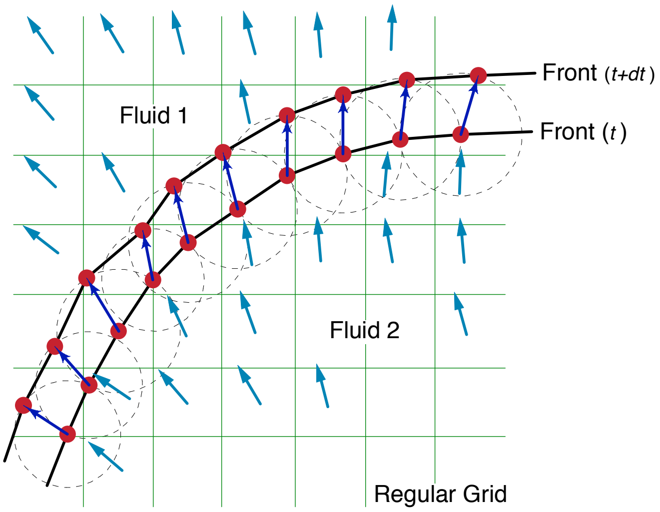

Figure 2.2: A two-dimensional front.

In many cases we wish to simulate periodic domains where the front can move out of the domain on one side and move in through the other side. In this case Eq. (2.41) must be modified to:

$$i = int(amod(x, L_x) \cdot NX/L_x) \tag{2.42}$$

2.2.2 Remeshing the front

In general, an interface will stretch and deform as a result of the fluid motion. When marker points are used to track the interface, stretching results in an increased separation of the points and eventually it is necessary to insert new points to resolve the interface adequately. When the interface is compressed, the points are crowded together and although it is, in principle, not necessary to remove points, in practice it is generally better to do this, in order to avoid the formation of elements much smaller than the grid size. To determine when it is necessary to add or delete an element, we define a minimum and a maximum element length. In two dimensions, 2-4 elements per grid mesh are recommended, see (Tryggvason et al. 2001).

In Figure 2.3 the addition and elimination of front elements of a two-dimensional system is shown. On the left side of the figure, a large element is split by the addition of a new element, and on the right side, an element is removed. In principle, the new point can be put at the mid point between the end points of the element that is being split or removed; but a better option is to take into account the curvature of the element and use a polynomial interpolation to determine the position of the new point.

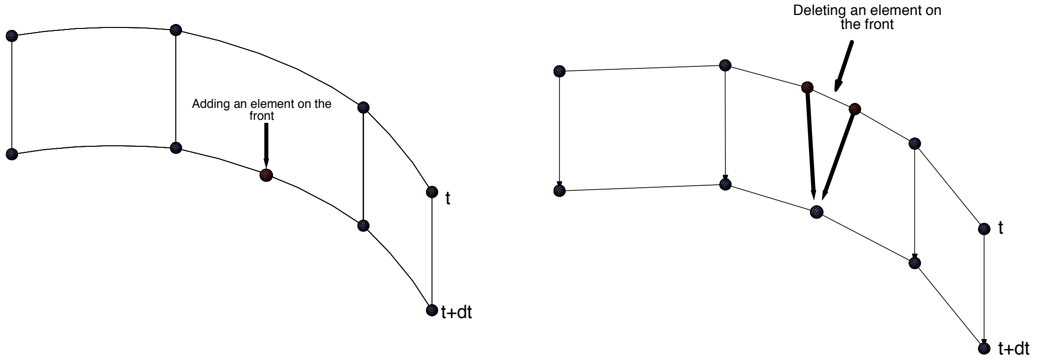

Figure 2.3: Adding and deleting front elements in two dimensions.

2.2.3 Interpolating the front properties onto the fixed grid

Since the Navier-Stokes equations are solved in the fixed grid and the interface forces like the surface tension are solved in the front, it is necessary to convert a quantity that exists in the front to a grid value. Since the front represents a δ function, the transfer corresponds to the construction of an approximation to this δ function on the fixed grid. The discrete expression required for the conversion of a quantity from the front to the fixed grid is given by:

$$\phi_{ij} = \sum \phi_l \omega_{ij}^l \frac{\Delta L}{h^2} \tag{2.43}$$

where ϕ_{ij} is an approximation to the grid value, ϕ_l is an approximation to the front value, ΔL is the length of the element l and ω_{ij}^l is the weight of grid point ij with respect to element l. The weighting functions can be written as a product of one-dimensional functions. In two dimensions the weight on the grid point (i, j) of the smoothing from $X_p = (x_p, y_p)$ is given by:

$$\omega_{ij}^l = d(x_p - ih)d(y_p - jh) \tag{2.44}$$

A bilinear interpolation can be used to construct $d(r)$ (Prosperetti & Tryggvason 2007):

$$d(r) = \begin{cases} (h - |r|)/h, & |r| < h \\ 0, & |r| \geq h \end{cases} \tag{2.45}$$

A geometric interpretation of Eq.(2.45) is shown in Figure 2.4. For distribution of a front property at x_p, the grid point (i, j) gets the fraction determined by A_1, the grid point $(i + 1, j)$ the fraction determined by A_2 , and so on.

For the present purposes, it is more convenient to use the weighting function developed by (Peskin 1977):

$$d(r) = \begin{cases} (1/4h)(1 + cos(\pi r/2h)), & |r| < 2h \\ 0, & |r| \geq 2h \end{cases} \tag{2.46}$$

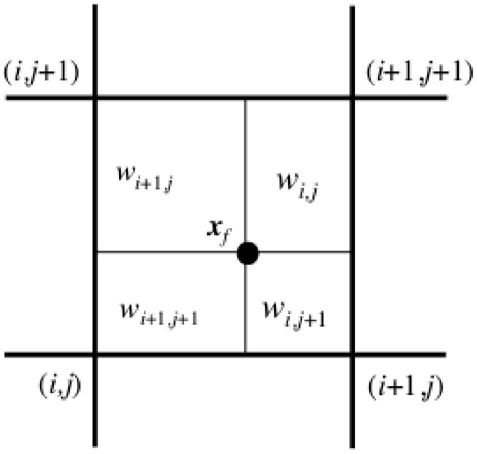

Figure 2.4: The area weighting used to interpolate grid quantities to the front.

While in the bilinear weighting function only four points are necessary to interpolate a quantity from the front to the fixed grid or vice versa, using the weighting function given by Peskin, sixteen points of the finite volume grid are affected for the quantity calculated on the front. The computational effort is rewarded with a smooth transition of properties between the front and the regular grid when the Peskin interpolation is used.

2.2.4 Computing the material properties

When front-tracking method is used, the boundary between the different fluids is moved according to the previously stated steps, but the fluid properties such as the density and viscosity, are not advected directly, and it is therefore necessary to reset these quantities at every time step. In order to make a consistent calculation, we first define a marker function $I(x)$ that is a constant within a fluid, but different for each fluid and then use it to set the physical properties. To construct the marker function we use the fact that the front marks the jump in the density and that this jump is translated into a steep gradient on the fixed grid. The gradient of the marker function in the one fluid formulation can be expressed as

$$\nabla I = \int \Delta I \mathbf{n} \delta(\mathbf{x} - \mathbf{x}_f) dL \tag{2.47}$$

Or in a discrete form can be written as

$$\nabla(I)_{ij} = \sum_l \Delta I \omega_{ij}^l \mathbf{n}_l \Delta L \tag{2.48}$$

The density field has been chosen as the marker function in many implementations, and once the grid gradient field has been constructed, the density field can be recovered. Taking the numerical divergence of the grid density gradient results in:

$$\nabla^2 \rho = \nabla \cdot \nabla(\rho)_{ij} \tag{2.49}$$

The left-hand side is approximated by standard centered differences, and solving the resulting Poisson equation with the appropriate boundary conditions yields the density field everywhere. It is important to note that the resulting Poisson equation only is solved on points close to the interface,leaving points away from the interface unchanged.The solution of the equation around the interface can be accomplished by a three-step process: First the interface cells are marked by looping over the front points and setting a flag for those cells through which the interface crosses. Second, a one directional linked list of the interface cells is generated by running through all the grid cells and linking marked cells. Finally, the marker function is found by solving the Poisson equation iteratively in the marked cells using the linked list to move from one marked cell to the next.

The field distribution $\phi(\mathbf{x}, t)$ of other fluid properties can be calculated with the marker function using a linear interpolation,

$$\phi(\mathbf{x}, t) = \frac{\phi_f(\rho(\mathbf{x}, t) - \rho_b) - \phi_b(\rho(\mathbf{x}, t) - \rho_f)}{\rho_f - \rho_b}. \tag{2.50}$$

where the subscripts b and f represent properties of the bubble and the surrounding fluid, respectively.

2.2.5 Moving the front

The advancing of the front must be found by interpolating from the fixed grid field velocity, using the same weighting function that was used to transfer the properties from the front to the fixed grid. Once the velocity of each front point is known, its new position can be found by a simple first order explicit Euler integration:

$$\mathbf{X}_f^{n+1} = \mathbf{X}_f^n + \mathbf{v}_f^n \Delta t, \tag{2.51}$$

where $\mathbf{X}_f$ is the front position, $\mathbf{v}_f$ is the front velocity, and Δt is the time step. It is important to comment that the front velocity is computed using the Peskin weighting function, i.e., the velocity of the sixteen closer points of the fixed grid to one point of the front are used to find its velocity.

Chapter 3

Numerical Simulations of bubble dynamics

In this chapter the numerical simulation of bubbles for various flow conditions is presented. First, the conventional dimensionless parameters used to characterize the rising of bubbles are defined, and a brief discussion on experimental results is given in order to have present in mind the expected results from the numerical calculations. Then, dynamical properties of the motion of the bubbles and the flow generated in the surrounding fluid obtained with the simulations for different flow conditions are presented in the following sections. Finally, a comparison of the numerical simulations with a simple theoretical model reported by (Pesavento & Wang Jane 2004) and with quasi-two dimensional experimental observations of bubble dynamics in a Hele-Shaw experiments obtained by (Ramos et al. 2007) is given.

3.1 Simulations of bubbles at low and moderate Reynolds number

3.1.1 Bubble shape results

Consider a fluid in the presence of a gravity force where a bubble is injected. Since the bubble has lower density than the surrounding fluid, the bubble ascends by buoyancy effect. In early literature, bubbles rising in a viscous fluid were grouped in three categories: "Spherical", in which the surface tension and viscous forces are much more important that the inertia forces. "Ellipsoidal", the name usually given to bubbles which are oblate with a convex interface around the entire surface, and "Spherical cap" or "Ellipsoidal cap", that are large bubbles that tend to adopt flat or indented bases and that lack any semblance of fore-and-aft symmetry. If the bubble has an indentation at the rear, it is often called "dimpled", large spherical- or ellipsoidal-cap may also trail thin envelopes of dispersed fluid referred to as "skirts". Modern qualitative classification of bubble shapes and dynamics are based on non dimensional numbers which reflect the dominant physical effects.

The four most useful dimensionless numbers, are the Reynolds, Morton, Eotvos and Archimedes numbers defined by:

$$
\begin{aligned}
Re &= \frac{\rho_f U_T D}{\mu_f}, \qquad & M &= \frac{g\mu_f^4}{\rho_f^2 \sigma^3} \\
Eo &= \frac{\rho_f D^2 g}{\sigma}, \qquad & Ar &= \frac{g D^3 \rho_f (\rho_f - \rho_b)}{\mu_f^2}
\end{aligned}
\tag{3.1}
$$

where U_T is the terminal velocity of the centroid of the bubble, μ_f is the viscosity of the continuous phase and D is the initial diameter of the bubble. Each dimensionless number is a relation of physical effects acting in the flow. The Reynolds number is the ratio of the inertia forces to the viscous forces, also it can be interpreted as a dimensionless velocity. The Eotvos number is a measure of the importance of surface tension forces compared to gravity force, the Morton number is the ratio of the gravity and viscous forces to the surface tension force and the Archimedes number represents the ratio of buoyancy and inertial forces. Note that the density difference between the fluids around the bubbles and that of the bubble itself is included in the Archimedes number. Another well known non dimensional number that is often useful in the studies of the formation of droplets and bubbles is the Weber number, it can be thought of as a measure of the kinetic energy compared to the surface energy, however, this number can also be expressed by using a combination of the other non dimensional parameters described above.

Many experiments of individual bubbles rising in a viscous fluid have been done for a wide range of flow conditions. The results presented in (Sanada et al. 2007) and (Bhaga & Weber 1981) are some examples of them. However, the most important reference in the bubbles experiments is the work of (Clift et al. 1978) in which a wide range of flow conditions were explored and reported. In Figure 3.1 the chart given by (Clift et al. 1978) is shown. The chart has been used to describe the qualitative shape of bubbles as a function of the dimensionless numbers mentioned above, the different categories of the shape of the bubbles are separated by a continuous line.

In this work, numerical simulations of bubbles were done for different physical conditions given in the shape chart described above; in figure 3.1, the blue dots denote the conditions simulated and described in this section. It is important to note that the numerical model described in chapter 2 was developed in two dimensions and the chart was constructed from real experimental observations and consequently, in three dimensional systems. However, in order to make a qualitatively validation of the model, the calculated shape of the bubble will be compared with the information contained in chart. The numerical solutions were obtained in a rectangular periodic domain with a grid of 400 x 480 in the x and y directions respectively, it is important to mention that a circular shape of the bubble was imposed as an initial condition for all the numerical simulations.

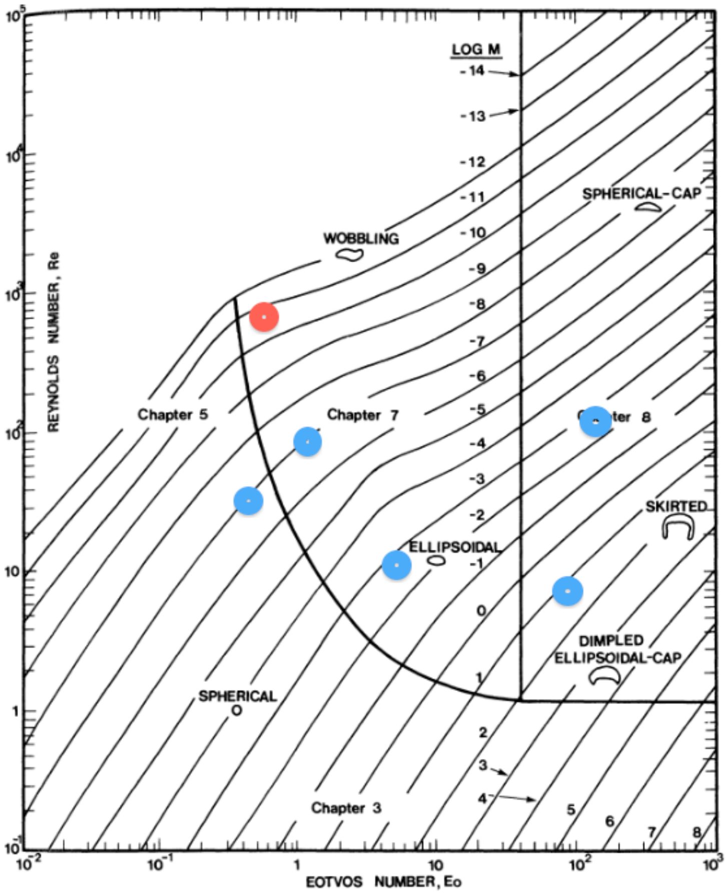

Figure 3.1: Shape regime for bubbles through liquids.

The bubble shapes predicted by our calculations are shown in Figure 3.2 for the flow conditions marked in the chart and as can be observed, even when the numerical simulations are in two dimensions and the chart is composed with three dimensional experimental information, the qualitative shape of the bubbles coincides in all cases. As it was described before, the bubbles rising in a fluid are classified in three groups, the simulation in a) the surface tension force dominates and the bubble adopts an spherical shape; in b) and c) the bubbles are elliptical because of Eotvos number is increased and the body and viscous forces begin to be the dominant effects. Finally, in d) and e) the elliptic-cap shape are presented and it is clear that case d) is a dimpled shape and e) a skirt shape in which the body and the viscous forces are much greater that the surface tension force. This is the shape that usually appears in large bubbles. The streamlines of the flow generated by the moving bubble are also given in Figure 3.2 for surface tension dominating flow (low Eotvos number) and for inertial dominating flow (large Eotvos number).

Simulation	Eo	M	Ar	Re_{sim}
a)	0.6	2.4×10^{-6}	300	24.0
b)	1.2	5.5×10^{-7}	1659	63.6
c)	7.2	1.2×10^{-2}	178	9.8
d)	64.8	1.8×10^{1}	122	5.3
e)	112.4	4.0×10^{-4}	24652	79.8

Table 3.1: Flow conditions of the numerical simulations.

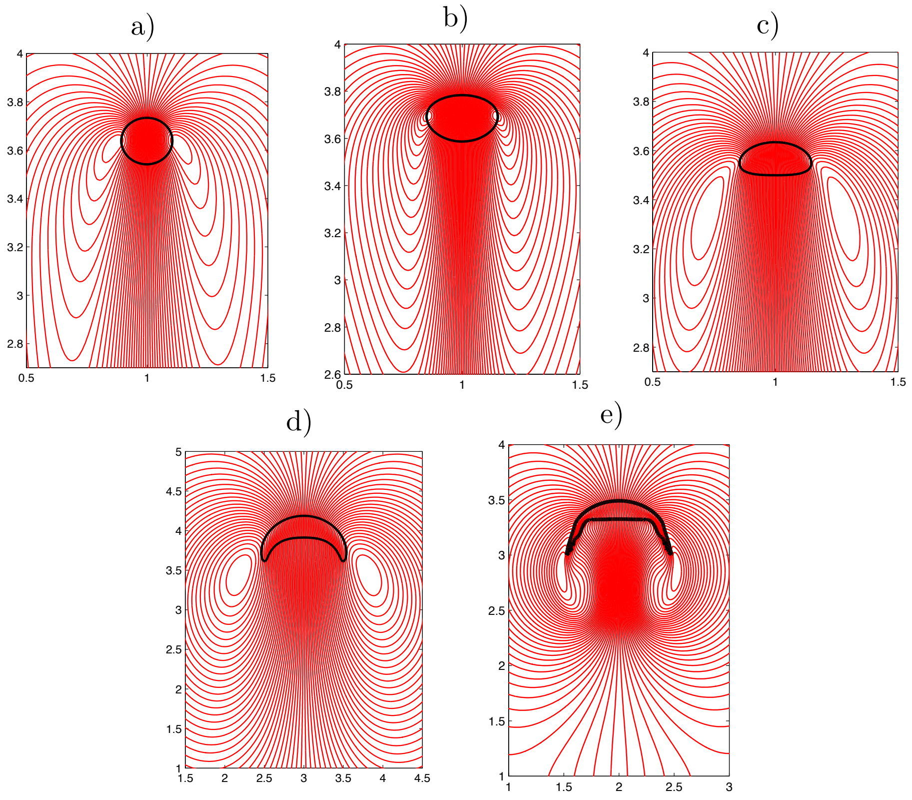

Figure 3.2: Bubble shapes and streamlines for different flow conditions. The nondimensional numbers used in each case are given in Table 3.1

It is well known that for bubbles rising in a viscous fluid, the path of the centroid of the bubbles is straight and the wake of the bubble is symmetric when the Reynolds number is low (Bhaga & Weber 1981). Experiments report that as the Reynolds number increases up to 110 the closed symmetric wake is replaced by an open, unsteady wake. This behavior is confirmed by the results presented in Figure 3.2, where it is clear that the wakes of the bubbles for the different conditions are symmetric and steady. This is due to the fact that the resulting terminal Reynolds numbers obtained from the simulations are low.

3.1.2 Rising velocity of the bubble

The velocity of the centroid is an important parameter for the description of the bubble dynamics and was computed with a similar algorithm as the one for the calculation of the velocity of every point of the front, using the weighting function to transfer the velocity in the fixed grid to the location that corresponds to the centroid of the bubble. The interpolation starts by identifying the grid point that is closest to the centroid of the bubble, then the grid value is calculated by:

$$u_c = \sum_{ij} \omega_{ij}^{c} u_{ij}, \tag{3.2}$$

where u_c is the velocity of the centroid of the bubble, ω_{ij}^{c} is the weight of grid point ij with respect to the centroid c and u_{ij} is the value of the velocity on the regular grid. The velocity of the centroid can be used to calculate the Reynolds number, provided that a definition for a characteristic magnitude of the bubble is available. In Figure 3.3 the Reynolds numbers for the flow conditions presented in the Table 3.1 are plotted. As it was mentioned the Reynolds number can be interpreted as a dimensionless velocity when the diameter of the bubble is a constant, the definition of the Reynolds number plotted is based on the initial diameter of the bubble. In Figure 3.3, it is clear that for low Reynolds number the bubble is accelerated in the first seconds of the simulations and after this fast acceleration it reaches a terminal velocity that remains constant while the bubble ascends in the column of fluid. However, as it can be seen, when the Reynolds number is increased, oscillations in the bubble velocity appears (see green curve of Figure 3.3). This behavior is brought about because the inertial forces dominate the flow and nonlinear effects are manifested. The cases in which the velocity of the bubble oscillates are reported in the next section of this work.

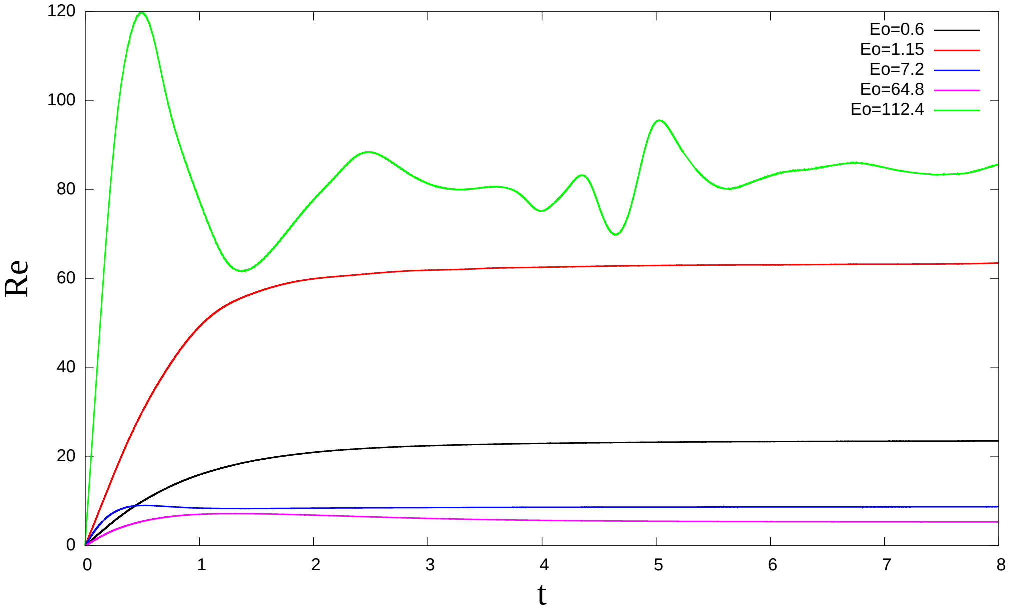

Figure 3.3: Reynolds number as a function of time.

Another parameter that can be used to complement the description of the dynamics of the rising bubbles is the Morton number. In Figure 3.4, the effect of the Morton number on the normalized terminal velocity is shown, keeping the Eotvos number constant $Eo = 1.6$, the terminal velocity of the bubble is normalized using the gravity acceleration g and the initial diameter of the bubble D. As it can be observed from the figure, the terminal velocity of the bubble is a monotonous decreasing function of the logarithm of the Morton number. Moreover, for small values of the parameter, $10^{-11} < Mo < 10^{-7}$, the terminal velocity is almost a constant. For larger values of the Morton number, $10^{-5} < Mo < 10^{-2}$ the terminal velocity is a linear function of the log Mo with negative slope. Since the Morton number can be interpreted as a measure of the viscosity of the surrounding fluid (if the Eotvos number is kept constant), then with the previous results we can conclude that the terminal velocity of the bubbles is strongly dependent of the viscosity of the fluid only in the cases where the bubbles rising in a very viscous fluid.It is important to emphasize that all results given in figure 3.4 were obtained for constant terminal velocity. For Morton numbers smaller than 10^{-11}, the velocity, and the Reynolds number, are large enough so that the bubble displays an oscillatory motion. This phenomenon will be discussed in the next section.

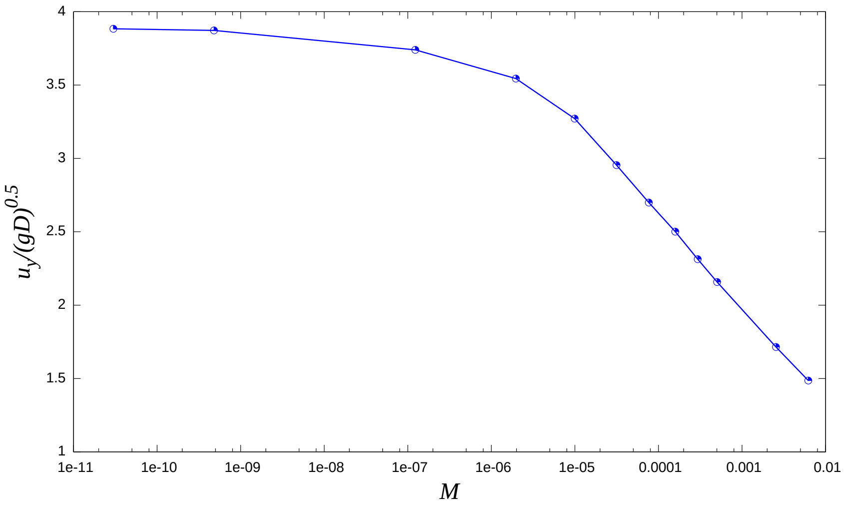

Figure 3.4: Effect of the Morton number on the terminal velocity of the bubble (Eo=1.6).

3.1.3 Flow around the bubble

For small to moderate Reynolds numbers, the flow formed around the bubble is a dipole vortex. For an example, see Figure 3.2 a), d) or e). The features of the dipole depend on the dimensionless parameters mentioned above, namely, the Eotvos and Morton numbers.

The analysis of the flow around the bubble was done by plotting the pressure and vorticity fields. To illustrate the disturbance that the transit of a bubble causes on the pressure field of the fluid, Figure 3.5 displays the pressure field for the parameters given in Table 3.1. It is important to remark that the pressure field, as well as the rest of the flow, is time-dependent in the frame of reference where the description is made and the figure gives a single snapshot captured when the bubbles were at the position shown . The hydrostatic pressure field can be identified as a gentle constant background pressure gradient. The surface tension forces on the bubble keep the pressure inside it nearly constant and higher than the ambient pressure. Also when the bubble is spherical (a) the center of the vortices are close to the bubble surface and the wake of the bubble is hardly distinguishable. However, when the bubble is ellipsoidal and ellipsoidal-cap (c,d,e) the center of the vortices move away from the bubble and the low pressure zones intensifies behind the bubble.

The corresponding vorticity fields are shown in Figure 3.6. Positive values of the vorticity indicate a counter-clockwise rotation of fluid elements viewed from the front while negative values represent a clockwise rotation. As it is expected, the strong zones of vorticity are at the centers of the dipole vortices, and since these simulations correspond to moderate Reynolds numbers, the vorticity distribution is steady and symmetric. In the next section, simulations where the vorticity symmetry is broken are presented.

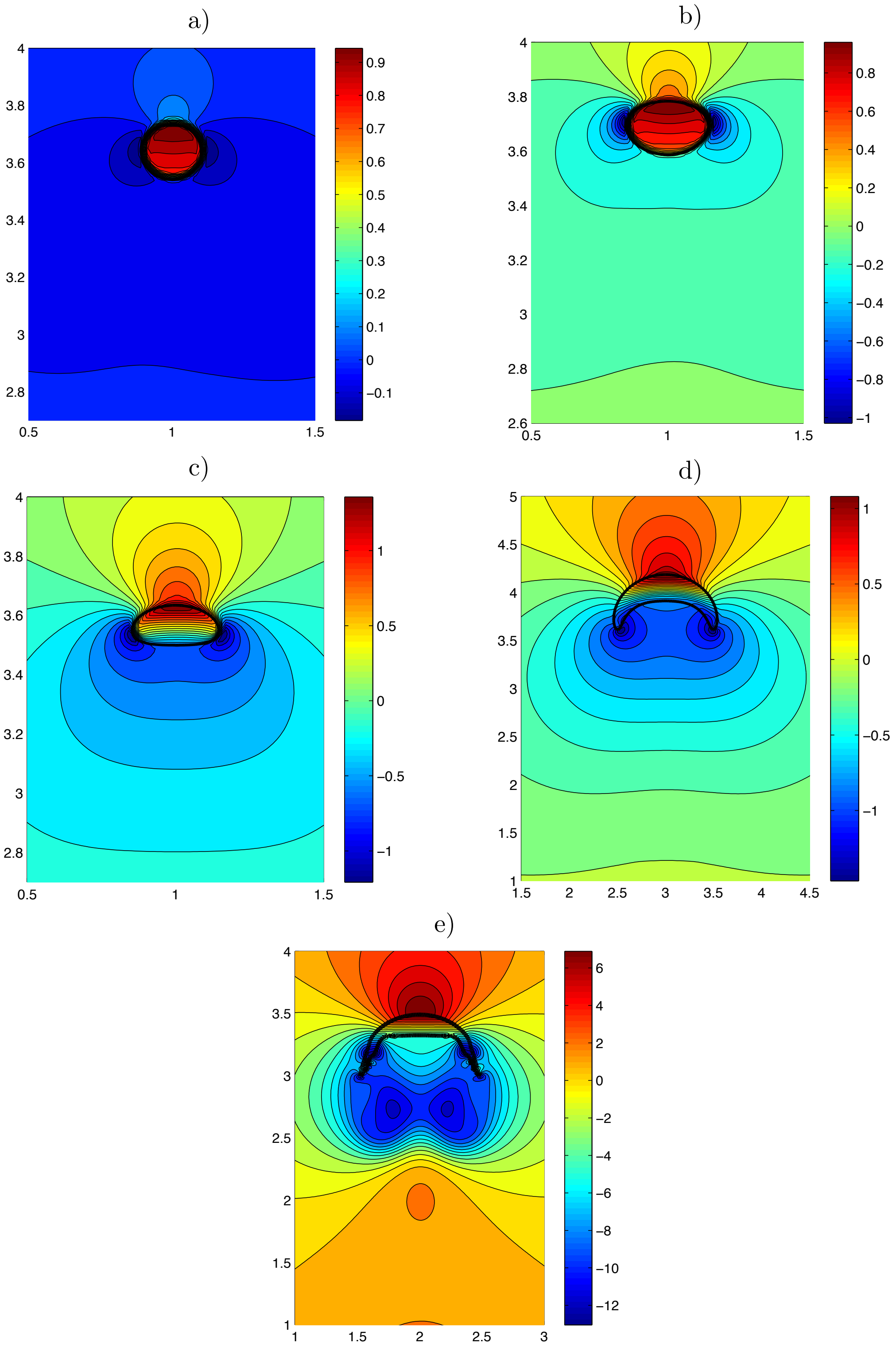

Figure 3.5: Bubble shapes and pressure fields for different flow conditions: a) $Eo = 0.6$, $Ar = 300$, $Re = 24$; b) $Eo = 1.2$, $Ar = 1659$, $Re = 63.6$; c) $Eo = 7.2$, $Ar = 178$, $Re = 9.8$; d) $Eo = 64.8$, $Ar = 122$, $Re = 5.3$; e) $Eo = 112.4$, $Ar = 24562$, $Re = 79.8$.

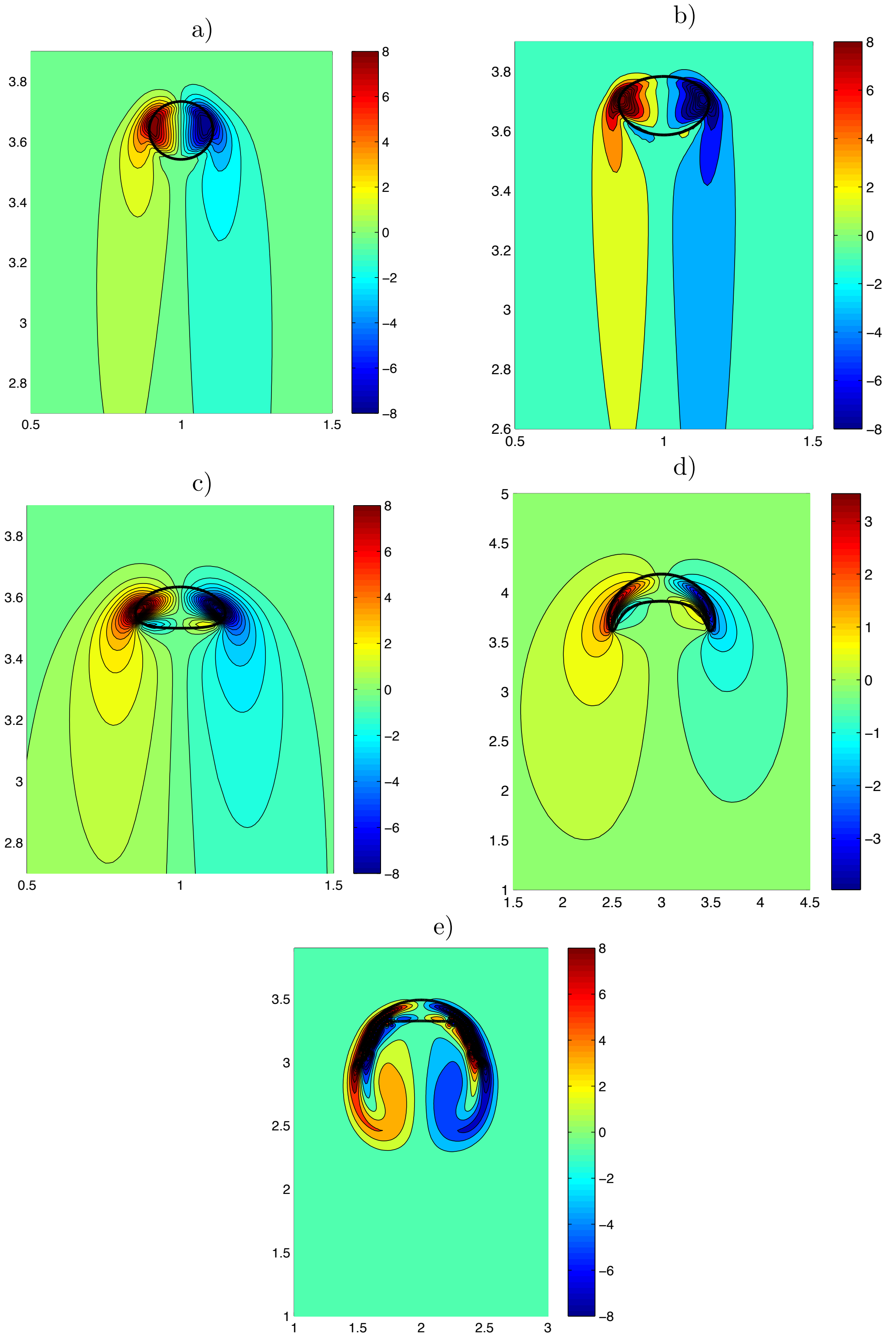

Figure 3.6: Bubble shapes and vorticity fields for different flow conditions: a) $Eo = 0.6$, $Ar = 300$, $Re = 24$; b) $Eo = 1.2$, $Ar = 1659$, $Re = 63.6$; c) $Eo = 7.2$, $Ar = 178$, $Re = 9.8$; d) $Eo = 64.8$, $Ar = 122$, $Re = 5.3$; e) $Eo = 112.4$, $Ar = 24562$, $Re = 79.8$.

3.2 Simulations of bubbles at high Reynolds numbers

3.2.1 Trajectory of the centroid and orientation of a single bubble

As it was commented in section 3.1, the trajectory of the bubble changes from a straight to a zig-zag path when the Reynolds number of the bubble exceeded a threshold. In the regime where bubbles exhibit approximately oblate spheroidal shapes, they rise in zigzag path. As the Reynolds number is increased, diffusion and convection of vorticity no longer keep pace with vorticity generation. Instead, discrete pockets of vorticity begin to be shed from the wake.

The Reynolds number at which vortex shedding begins is often called the “lower critical Reynolds number” (Clift et al. 1978), but the transition is much more gradual than this label would imply. The transition from a straight path to a zig-zag path starts with small oscillations along the trajectory of the bubble, the oscillations appear only in some intervals of time (see green curve in Figure 3.3), as the Reynolds increases, the oscillations are more pronounced and a clear periodicity in the motion of the bubble is apparent. This kind of transition is very similar to the transition occurring for high Reynolds numbers in the flow over a rigid cylinder. In such flow wake oscillation is apparent for $Re > 30$, and wake shedding for $Re > 40$. Shedding from a cylinder gives a regular succession of vortices, called the ”von Kármán vortex street”. However, the unsteady flow that appears around the bubble is more complex because the deformation of the bubble is coupled with the flow around it and vice versa.

The dynamics of the bubble wake at such flow conditions may have a crucial effect on the path of the bubble, as periodic vortex shedding has been proved to have on the path of two-dimensional bubbles rising in a Hele-Shaw cell (Kelley & Wu 2005). In this work numerical simulations were done in order to explore the features of the bubble at this regime. It is convenient to show the numerical results in terms of the following dimensionless variables:

$$x^* = \frac{x}{D}; \quad y^* = \frac{y}{D}; \quad u^* = \frac{u}{(Dg)^{\frac{1}{2}}}; \quad t^* = \frac{t}{D^{\frac{1}{2}} g^{-\frac{1}{2}}}; \quad p^* = \frac{p}{\rho_f g D}, \tag{3.3}$$

The simulation parameters must be adjusted to get physical conditions that render a motion with a high enough Reynolds number, an oscillatory bubble and a zig-zag trajectory. In the present context, the most convenient set of dimensionless numbers must include the Archimedes number, since this parameter contains the density difference between the two fluids and the velocity of the bubble (and the Reynolds number) is a direct function of the density difference.

In Figure 3.7, the trajectories of the centroid of bubbles are drawn for $Eo = 0.54$ and $M = 2.5 \times 10^{-11}$and three different Archimedes numbers. It is important to note that for purposes of clarity, the abscissa has been greatly enlarged with respect to the ordinate. Analyzing the features, the trajectory in which $Ar = 78401$, it is observed that after an initial transient that takes approximately $20D$, the motion is oscillatory with a fast mode that completes a cycle in $12D$ and a slow mode with a cycle of $40 - 50D$. The zig-zag motion is generated by the asymmetry of the pressure field in the periphery of the bubble which in turn results from the fact that the surface of the bubble deforms in response to the external field of stresses.

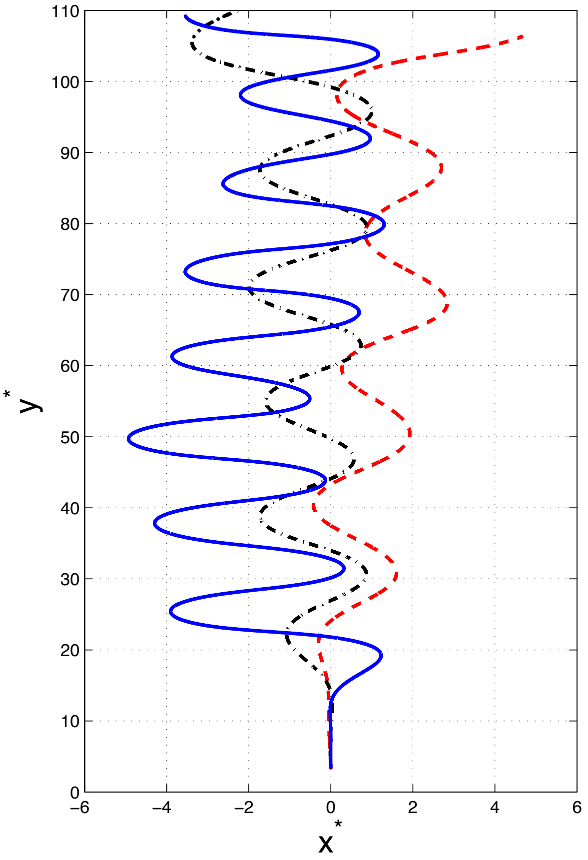

Figure 3.7: Trajectory of the centroid of the bubble for $Eo = 0.54$ and $M = 2.5 \times 10^{-11}$: $Ar = 59395$ (dashed red curve), $Ar = 63354$ (dashed black curve) and $Ar = 78401$ (continuous blue curve).

As it is illustrated in Figure 3.7, the amplitude of the oscillations is strongly dependent on the Archimedes number. Increasing this parameter the amplitude grows considerably. In order to analyze the characteristic frequencies, a Fourier transform was applied to the signals of the trajectories and the power spectra for them were found. In Figure 3.8 the power spectra of the signals are plotted. It is clear that increasing the Archimedes number, the oscillation frequency of the trajectory of the bubble increases.

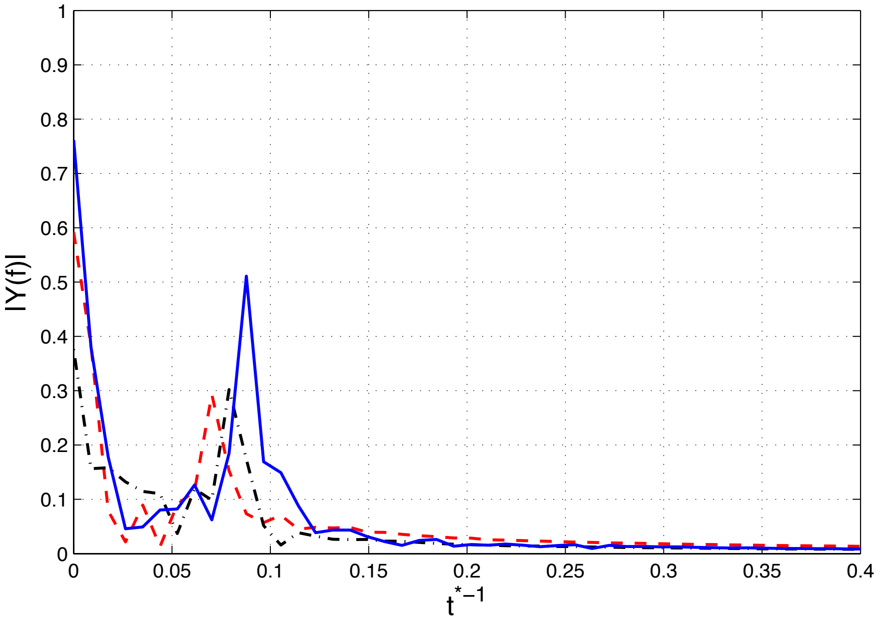

Figure 3.8: Power spectrum of the centroid trajectories of the bubbles for different Archimedes numbers and $Eo = 0.54$ and $M = 2.5 \times 10^{-11}$: $Ar = 59395$ (dashed red curve), $Ar = 63354$ (dashed black curve) and $Ar = 78401$ (continuous blue curve).

In order to document and quantify the last observation in the previous paragraph, simulations for different Archimedes numbers, keeping constant the other dimensionless parameters were done and the results are shown in Figure 3.9. For the low range of Archimedes numbers explored ($Ar < 6 \times 10^4$), the frequency of the bubble motion is almost a linear function of Ar; but the curve seem to approach the approximate asymptotic value of 0.088 for $Ar > 7 \times 10^4$. Since the other parameters were kept constant in the simulations, the Archimedes number can be translated as the density difference of the fluids, then the previous results imply that the motion of the bubble is almost independent to the density difference when the Archimedes number exceeds a threshold ($Ar > 7 \times 10^4$).

To further explore the dynamics, the instantaneous non-dimensional centroid velocity for the horizontal and vertical motions are given in Figure 3.10 for $Ar = 78401$. The vertical velocity oscillates around an averaged value of 1.3, while the horizontal velocity presents an almost periodic behavior with zero average value. The oscillation frequency of the vertical velocity is twice that of the horizontal velocity and its amplitude is approximately 0.75 while that of the horizontal velocity is larger than 3. Also, a crest of the horizontal velocity always corresponds to a trough of the vertical velocity.

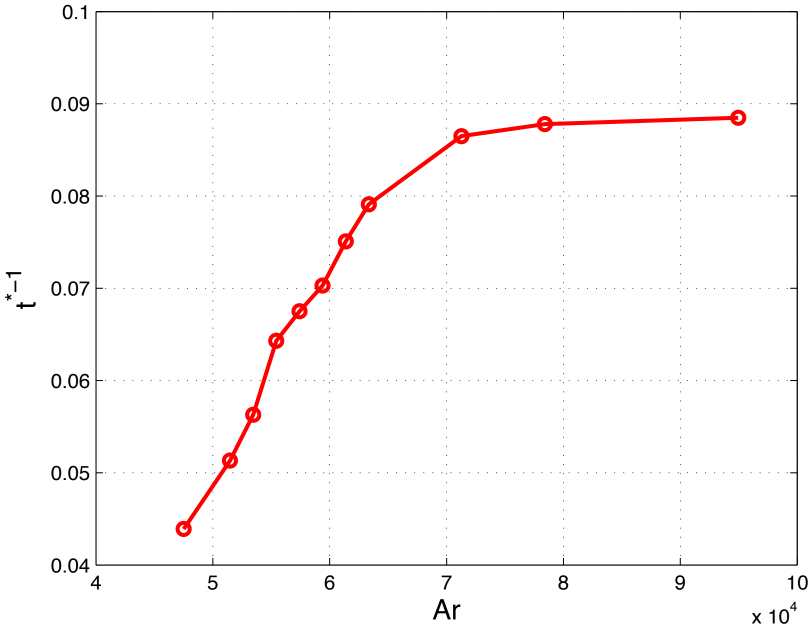

Figure 3.9: Effect of the Archimedes number on the oscillation frequency of the trajectory of the bubble ($Eo = 0.54$ and $M = 2.5 \times 10^{-11}$).

The dynamical features of the motion can be interpreted in terms of the inclination of the bubble as it ascends. Incidentally, the instantaneous position of the bubble could be computed by using an ellipse fit to the bubble, since for the non-dimensional parameters chosen, it can be concluded that the bubble shape always can be accurately approximated by an an ellipse since the flow regime is surface tension dominating. In the central panel of Figure 3.11, the inclination of the major axis of the bubble with respect to the horizontal in one cycle is shown. The bubble has a positive inclination in A) and a negative inclination in B), the pressure fields near the bubble are plotted for these conditions in the left and right panels. The pressure difference between two contiguous isolines is constant. The maximum angle of inclination of the bubble was about 45 °. This tilt motion is consistent with a non-symmetric pressure field around the surface of the bubble and with a periodically varying drag.

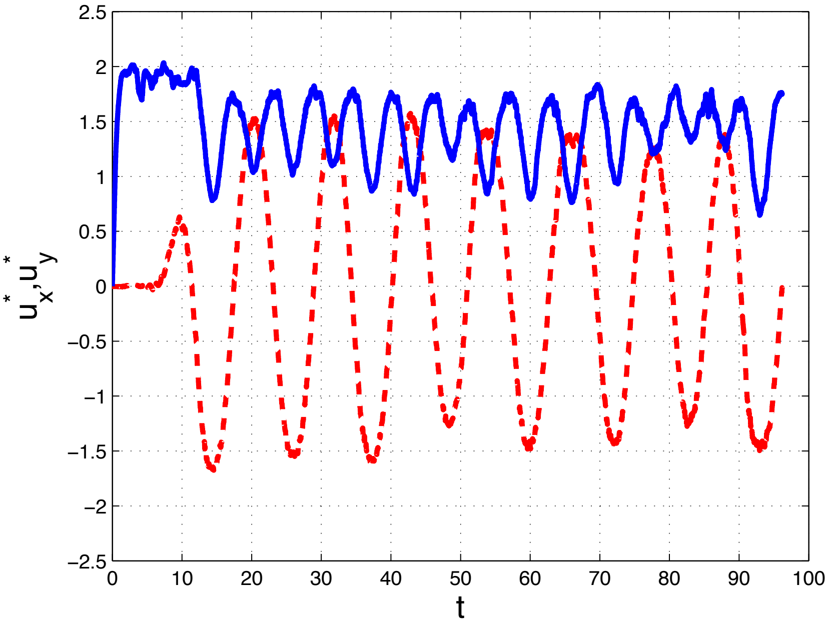

Figure 3.10: Instantaneous horizontal (dashed line) and vertical (continuos line) non-dimensional velocities.

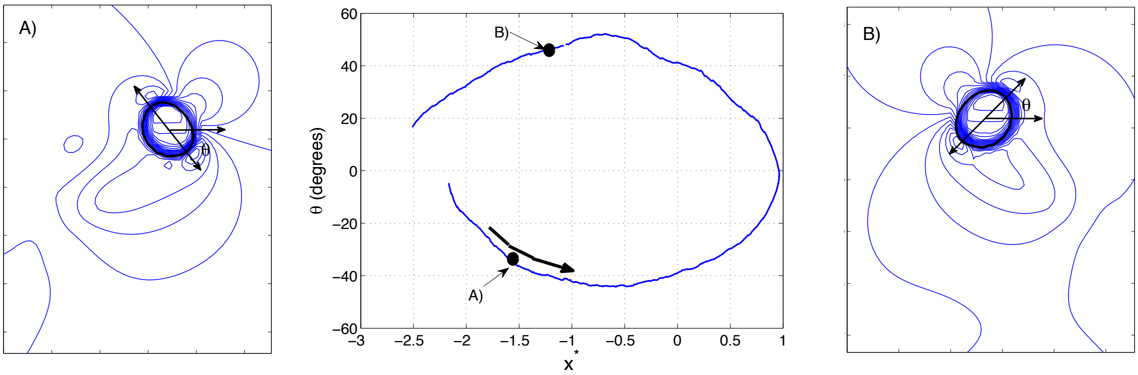

Figure 3.11: Inclination of the major axis of the best elliptic fit of the bubble in one cycle. See Figure 3.7. The arrow indicates the direction of time.

3.2.2 Flow around the bubble

A snapshot of the velocity, pressure and vorticity fields in the wake of the ascending bubble are shown in Figure 3.12. The most conspicuous feature observed in Figure 3.12 is that vortices are created on the lee side of the bubble and detach periodically from either side. This collection of vortices is similar to the Von Kármán vortex street generated by a rigid cylinder in relative motion with respect to a fluid.

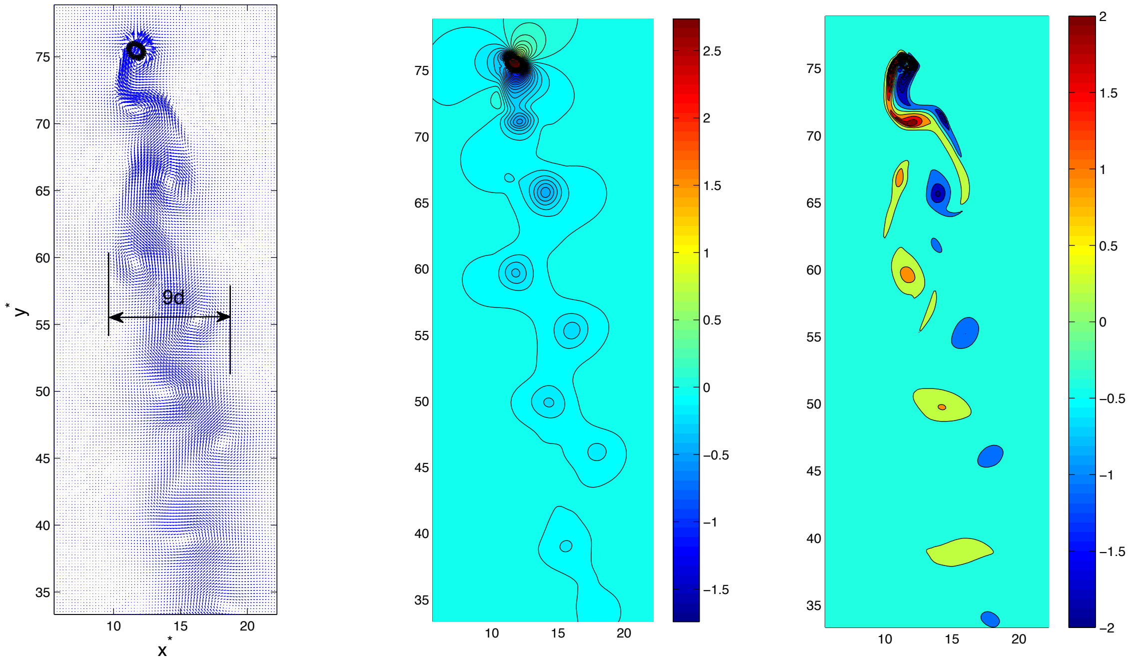

Figure 3.12: Velocity, pressure and vorticity fields. The vortex shedding can be observed in the wake of the bubble similar to the Von Kármán vortex street. In the vorticity field the intensity of the vortices is also displayed.

The dynamics of the bubble rising is closely related to its wake structure. A somewhat detailed study of the wake of a rising bubble is illustrated in Figure 3.12, which shows the velocity field around the bubble and a pressure contour in the bubble wake. When the bubble rising velocity is low, a bubble wake with symmetric, closed recirculation rings is formed, and a low pressure zone is generated at the recirculation centre as shown in the simulations of the previous section. As the rise velocity increases, the flow instability is amplified and the bubble wake starts to detach from one side of the bubble lower half as shown in the left panel of Figure 3.12. Due to the asymmetric wake structure, the drag and lift forces acting on the bubble will also become unbalanced, and the bubble is tilted (see the description of Figure 3.11). As a result, the recirculation ring of the bubble wake is fully broken on one side, and the other end of the recirculation ring starts attaching itself to one end of the ellipsoidal bubble. The lateral motion makes the open recirculation rings in the bubble wake to switch from one side to the other of the bubble lower half.

3.3 Comparison with a phenomenological model

In the previous sections, the analysis of the bubble motion was based entirely on the numerical solutions of the equations that describe the phenomenon. In order to gain physical insight and clarify which are the dominant effects, in the present sections we take advantage of the phenomenological model developed by Wang and her colleagues (Pesavento & Wang Jane 2004) to interpret our results in terms of the forces that have been traditionally identified as relevant in describing the motion of blunt bodies through a fluid. The discussion in this section is restricted to the analysis of the trajectory of the bubble centroid which is the only feature of the problem that is described by the phenomenological model.

The theoretical model considers the two-dimensional dynamics of an elliptic rigid body falling in a fluid and includes contributions from added mass, lift, and drag. The geometry and axes of coordinates are given in Fig. 3.13. The Reynolds number is based on the semi-major axis and the average velocity of the body is assumed to be of the order of 10^3. The quadratic lift and drag terms in the model are designed to describe the aerodynamics at intermediate Reynolds numbers between 10^2 and 10^3. This range of parameters gives us the opportunity to use this analysis to compare the results with the ones discussed in section 3.2.

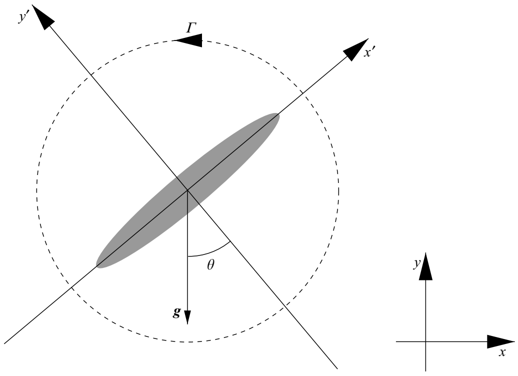

Figure 3.13: Physical model

Given that the interpretation demands a certain amount of detail, we give a brief description of the model, and stick to the nomenclature of the original authors. The phenomenological model is comprised by a set of coupled ordinary differential equations of motion that incorporates with individual expressions the fluid force contributions of buoyancy, added mass, lift and drag.

$$(m + m_{11})\dot{u_x} = (m + m_{22})\dot{\theta} u_y - \rho_f \Gamma u_y - \pi(\rho_b - \rho_f)abg \sin\theta - F_x \tag{3.4}$$

$$(m + m_{22})\dot{u_y} = (m + m_{11})\dot{\theta} u_x + \rho_f \Gamma u_x - \pi(\rho_b - \rho_f)abg \cos\theta - F_y \tag{3.5}$$

$$(I + I_a)\ddot{\theta} = (m_{11} - m_{22})u_x u_y - \tau \tag{3.6}$$

where u_x, u_y are the horizontal and vertical velocity of the centroid of the ellipse, θ is the inclination angle, ρ_f and ρ_s are the density of the fluid and the elliptical body, respectively, a and b are the semi-major and semi-minor axis of the ellipse, Γ is the circulation that is proportional to the lift force and is orthogonal to the direction of the motion, F is the drag that is opposite to the direction of the motion, and τ is the dissipative torque and is opposite to the direction of rotation of the ellipse body.

The additional coefficients m and I in the system of equations are the mass and the moment of inertia per unit length respectively:

$$m = \pi \rho_s ab; \qquad I = \frac{1}{4}\pi \rho_s ab(a^2 + b^2). \tag{3.7}$$

Also, the added mass coefficients $m11$ and $m22$, and the added moment of inertia, I_a, for the elliptical object considered in the model are given by:

$$m_{11} = \pi \rho_f b^2; \quad m_{22} = \pi \rho_f a^2; \quad I_a = \frac{1}{8}\pi \rho_f (a^2 - b^2)^2 \tag{3.8}$$

With this model, it is found that the circulation for fluttering and tumbling in the Reynolds number range between 10^2 and 10^3 depends on both the translational speed and the angular velocity of the ellipse:

$$\Gamma = -2C_t a \frac{u_x u_y}{\sqrt{u_x^2 + u_y^2}} + 2C_r a^2 \dot{\theta} \tag{3.9}$$

where C_t and C_r are dimensionless coefficients for the translation and rotation terms of the circulation respectively, and those coefficients were found for different flow conditions by (Andersen, Pesavento & Wang Jane 2005)

.

The drag and the dissipative torque depend on the Reynolds number.The drag force and the dissipative torque are calculated with the model proposed by (Wang Jane, Birch & Dickinson 2004):

$$\mathbf{F} = \rho_f a \left[A - B \frac{u_x^2 - u_y^2}{u_x^2 + u_y^2} \right] \sqrt{u_x^2 + u_y^2}(u_x, u_y) \tag{3.10}$$

where A and B are dimensionless constants. For the dissipative torque we use an expansion to second order in the angular velocity:

$$\tau = \pi \rho_f a^4 \left[\frac{U}{L}\mu_1 + \mu_2 |\dot{\theta}| \right] \dot{\theta} \tag{3.11}$$

where L is the characteristic length scale, equal to the semi-major axis in our case, U is the characteristic velocity scale, and μ_1 and μ_2 are dimensionless constants.

In order to validate the implementation of this model, the results obtained by (Andersen et al. 2005) were fully reproduced by the different parameters reported by the authors. As it was previously mentioned, the model was developed for a rigid ellipse, but it can be used with deformable bodies as bubbles provided that the shape of the bubble is included as a function of time. The required information of the bubble geometry can be extracted on each time step from our numerical simulation and fitting the shape with an ellipse, the major and minor axis (a and b) of the bubble can be identified as functions of time. In turn, these values are fed in the system of ordinary differential equations (3.4)-(3.6) which are solved with an explicit Runge-Kutta method to obtain the velocity of the centroid and the angular velocity of the bubble. The ellipse fit is valid because the flow conditions considered yield a surface tension dominated bubble that acquires an approximately elliptic shape.

In Figure 3.14, the trajectory of the bubble calculated in the numerical simulation is compared with the trajectory given by the model described in this section. As it can be observed, the general behavior shows a good qualitative agreement , with the amplitude and the frequency of the oscillation displaying almost quantitative agreement. The horizontal and vertical velocities are plotted in Figures 3.15 and 3.16, demonstrating the consistency of the two approaches.

Since the bubble behavior is in agreement with the numerical simulations, the phenomenological model can be used to analyze the different effects caused by the forces that dominate the motion of the bubbles. It must be observed that in the numerical simulations, all effects are contained in the Navier-Stokes equations, and in order to compare with a phenomenological model, one must single out the particular effect on the bubble.

In Figure 3.17, the individual effects of drag, buoyancy, lift and mass (for definitions, see equations (3.4)-(3.6)), obtained with the numerical calculation are plotted. As it can observed, the drag force (F_D) has similar features than the velocity of the bubble centroid; this behavior can be understood from the fact that the drag force is induced by the buoyancy force that causes the rising of the bubble in the column of fluid and is calculated through the components of the velocity given by Eq (3.10). The buoyancy force (F_B) displays a sinusoidal behavior, with the frequency of the vertical component twice as that of the horizontal component. The sinusoidal behavior is coupled with the oscillating angle of attack. As it was shown in the previous section (Figure 3.11), the angle takes values from -45° to 45°. The horizontal motion promoted by the buoyancy force has a typical behavior of a sine function with variable amplitude because of the deformation of the bubble. The vertical buoyancy force oscillates around 0.75, which is the average value of the vertical force that is responsible for the most important motion. However its amplitude is variable too, due to the deformation of the bubble that changes the semi-major and semi-minor axis of the bubble in each time step. The lift force (F_L) depends of the circulation around the bubble and is strongly affected by the deformation of the bubble; this effect is most noticeable in the vertical component. As in the drag and

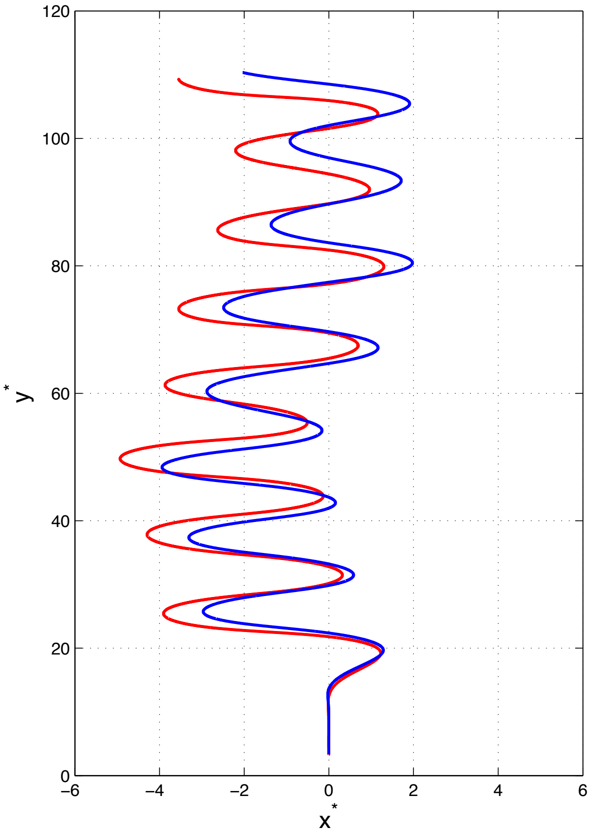

Figure 3.14: Comparison of the centroid trajectory obtained from the numerical simulation with the phenomenological model ($Ar = 78401$ and $Eo = 0.54$), numerical solution (red curve) and phenomenological model solution (blue curve).

buoyancy forces, the average value of the horizontal lift force is almost zero. The vertical component is always negative, which leads us to conclude that the lift force acts always as a brake on the ascendant motion of the bubble. In contrast, the effect of the mass added force (F_{AM}) seems to counteract that of the lift force. The vertical mass added force is always positive and has approximately the same magnitude that the vertical lift force.

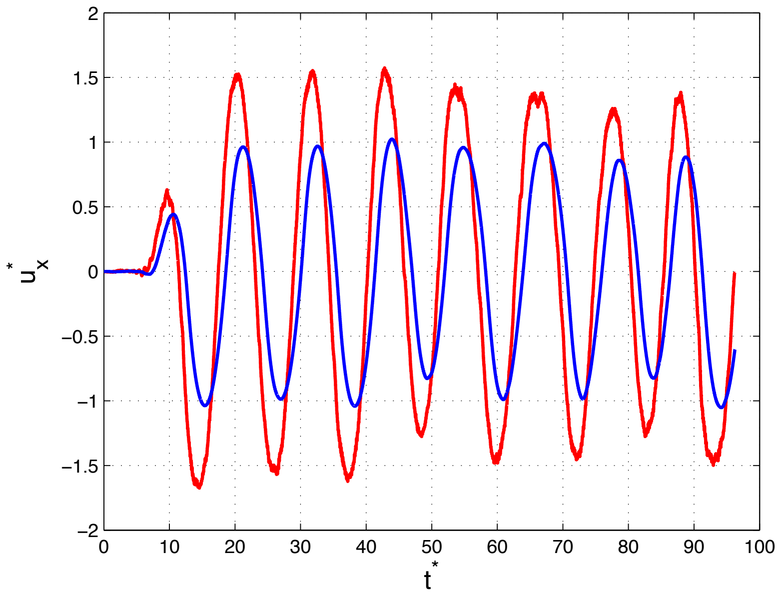

Figure 3.15: Comparison of the horizontal centroid velocity obtained from the numerical simulation with the phenomenological model ($Ar = 78401$ and $Eo = 0.54$), numerical solution (red curve) and phenomenological model solution (blue curve).

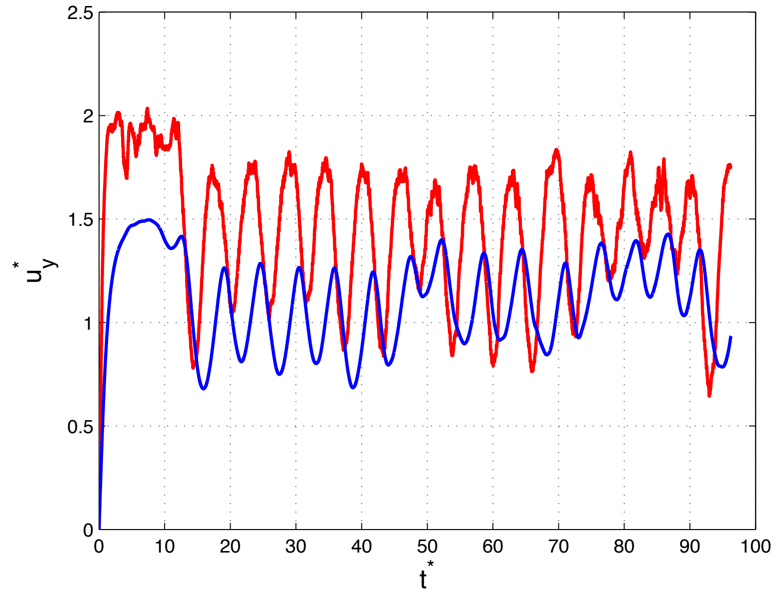

Figure 3.16: Comparison of the vertical centroid velocity obtained from the numerical simulation with the phenomenological model ($Ar = 78401$ and $Eo = 0.54$), numerical solution (red curve) and phenomenological model solution (blue curve).

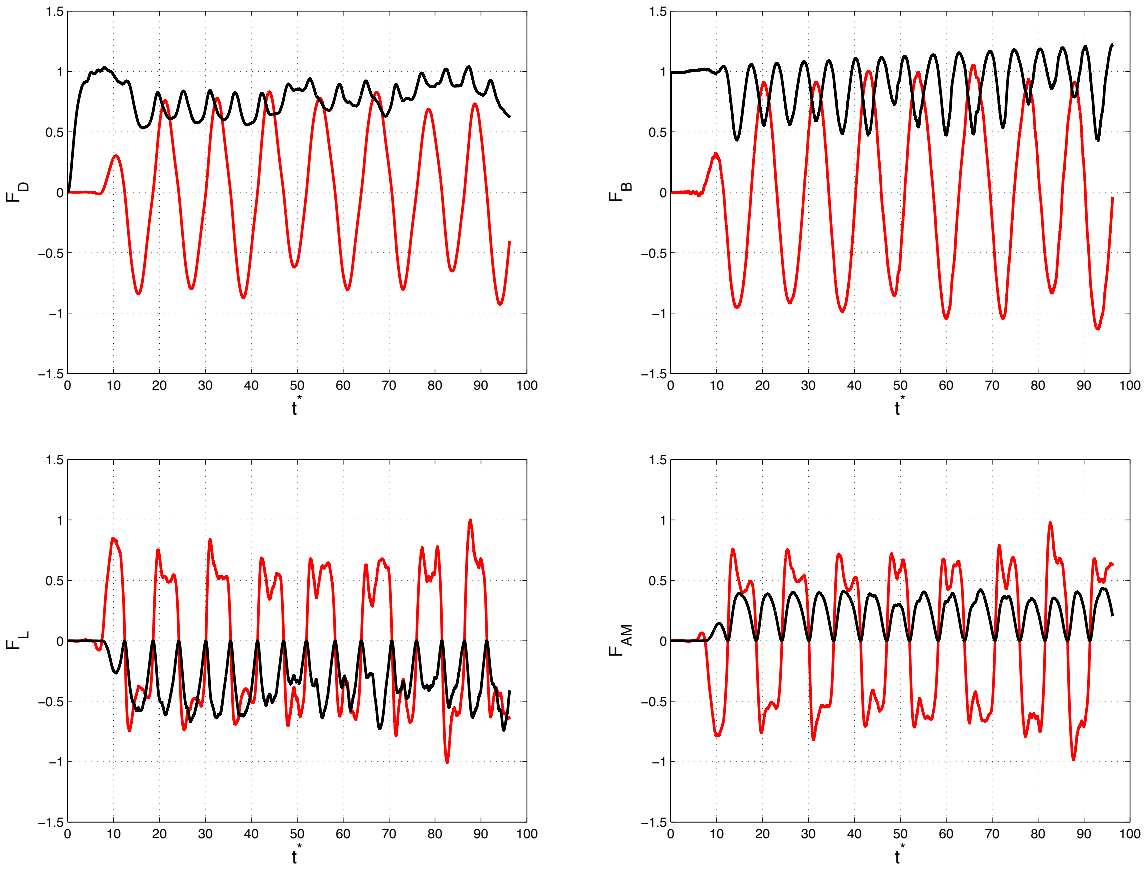

Figure 3.17: Computed fluid forces, the red curves are the horizontal components of the forces and the black curves are the vertical components of the forces.

3.4 Comparison with Hele-Shaw experiments

Since the model built in the present project is restricted to two dimensions, it is not completely possible to compare the results of our simulations with experiments. However, if the experiments are done in a quasi-two dimensional system, the bubbles will be necessarily constrained to move in a plane and then the results of our model could be compared with those experimental observations.

There are experiments of quasi-two dimensional bubble motions available in the literature which can be used to compare the front tracking model (Ramos et al. 2007). The experimental observations were done in a water filled Hele-Shaw cell [1] where bubbles were injected. The area of the observations was 77 bubble diameters above the bubble injector, where the influence of initial details was not relevant. Also, the width of the cell was about 67 diameters and it was expected that the effects induced by the lateral ends of the cell had a negligible influence on the bubble motion. A geometrical feature of the experimental devise that is markedly different from the simulations is that the presence of the cell plates that constrain the motion to be in two dimensions, do exert a drag force on the bubbles. The shape of the experimental bubbles was ellipsoidal, and the flow conditions in terms of the dimensionless parameters were $Ar = 78401$, $Eo = 0.54$ and $M = 2.5 \times 10^{-11}$.

In Figure 3.18, the experimental trajectory of the bubble in the Hele-Shaw cell for two and a half cycles is shown. As can be observed, the qualitative agreement with the simulations is satisfactory, but the model overestimates the velocity yielding an oscillation with larger amplitude and smaller frequency.

The lack of quantitative agreement can be attributed to the wall effects of the plates on the bubble motion. In the experiments, the bubble contained in the Hele-Shaw cell is flattened by the two glass plates; this causes shear stresses in the gas particles of the bubble that are in contact with the walls, exerting an extra drag. Another possible cause that makes the simulations to overestimate the dynamics of the bubble is the fact that the drag force on the surrounding fluid contained in the Hele-Shaw cell is larger than in free space. The fluid displaced by the transit of the bubble must move under the constraint of two rigid plates separated by a small gap.

A similar comparison with the experimental information available is shown in Figure 3.19, where the centroid trajectory is shown for one cycle and a better experimental time/space resolution. Again, the qualitative behavior is correctly modeled, but the scales are not the same. A plot of the vertical position as a function of time gives useful information on the major characteristics of the phenomenon as can be appreciated from Figure 3.20.

---

[1] A Hele-Shaw cell, consists of two parallel rectangular glass plates, separated by a thin gap where a viscous fluid is placed.

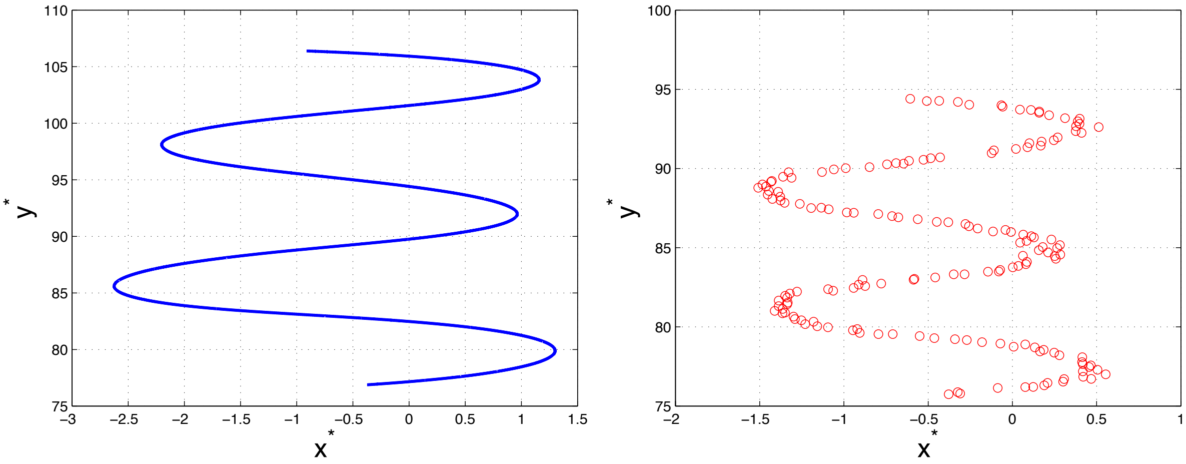

Figure 3.18: Comparison for the trajectory of the bubble with experiment in a Hele-Shaw cell (left side numerical simulations, right side experimental observations).

In experiments as well as in the simulations, the position is a wavy line that can be approximately represented by a straight line; the slope of this line is the average vertical velocity. The average vertical velocity in the computational simulations is about twice the velocity reported from the experimental information. The quantitative mismatch is again interpreted as the failure of the model to incorporate the effect of the glass plates. The waviness of the trajectory displayed in Figure 3.20 is better described in the frame of reference of a system that travels with the average vertical velocity. A result obtained in this way is given in Figure 3.21 where the orbit of the centroid of the bubble in the $(x, y - y_{ave})$ space is shown. The results of the simulation are in qualitative agreement with the experimental data with quantitative differences similar to those that have been discussed previously.

Another feature of the bubble dynamics calculated from the model that can be compared with the experiments is the orientation of the bubble. As it was commented before, this was computed using an ellipse fit over the bubble. In Figure 3.22, this feature is illustrated; and as can be seen, the orientation computed by the model is in full agreement with the experimental observations.

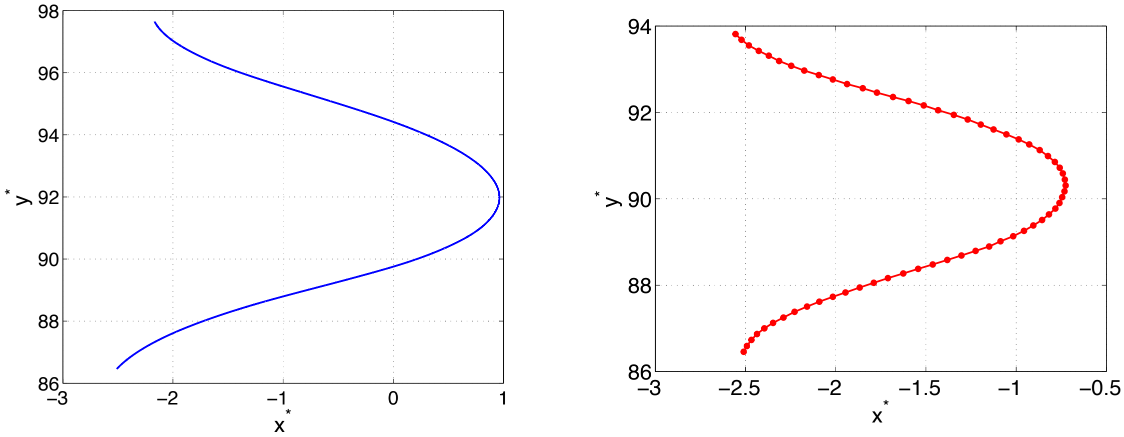

Figure 3.19: Trajectory of the centroid of the bubble in the plane (left panel, numerical simulations; right panel, experimental observations).

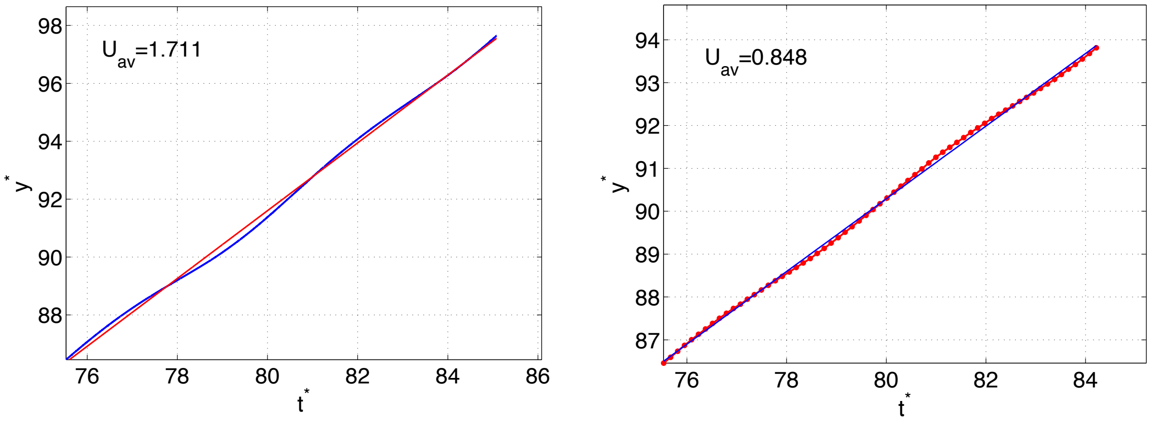

Figure 3.20: Vertical trajectory of the bubble (left side numerical simulations, right side experimental observations).

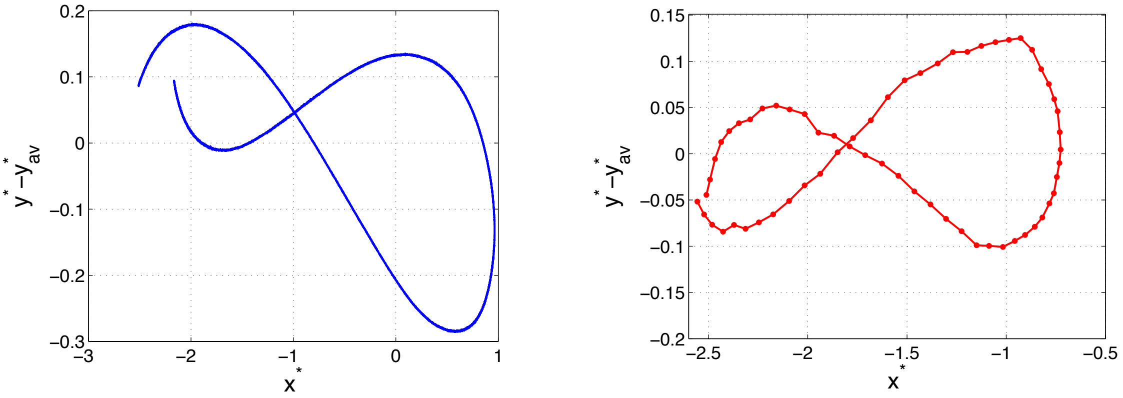

Figure 3.21: Trajectory of the bubble in a reference system traveling with the average vertical velocity (left side Numerical simulations, right side Experimental observations).

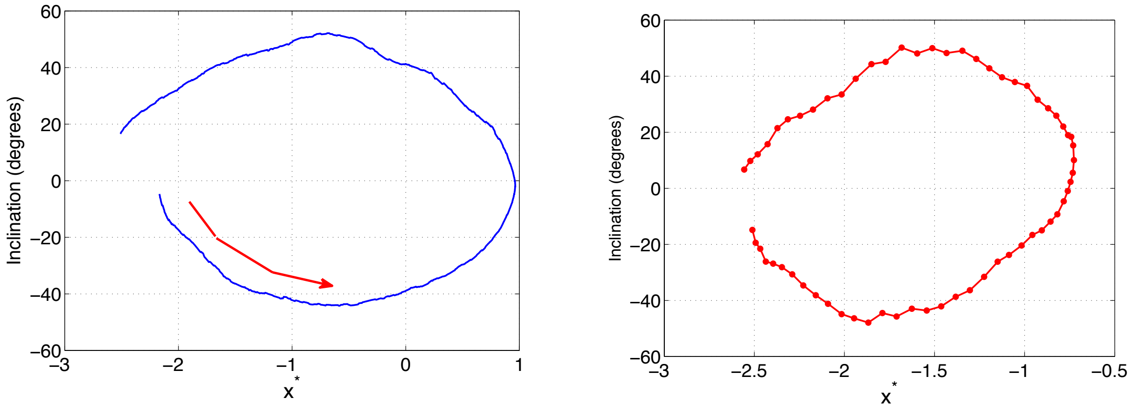

Figure 3.22: Orientation of the bubble (left side numerical simulations, right side experimental observations).

The external flow generated by the motion of the bubble can be predicted with the model and compared with the experimental observations as is illustrated in Figure 3.23. In the two cases, the flow displays a structure akin to the von Kármán vortex street. In the experiments, the vortex shedding in the wake of the bubble is clearly appreciated, and plotting the velocity field obtained from the numerical simulation, the vortex shedding is also visualized, but an interesting difference between the experimental results and the numerical simulation is that the vortices in the experiment dissipate faster than in the simulation. This can be explained again by the friction of the water with the walls causing a rapid vortex dissipation. Comparison other than qualitative is difficult at this point since the visualization is only qualitative. It is important to highlight though, that in the experiments the width of the Von Kármán vortex street is about 7 diameters and in our numerical simulations the width is about 9 diameters.

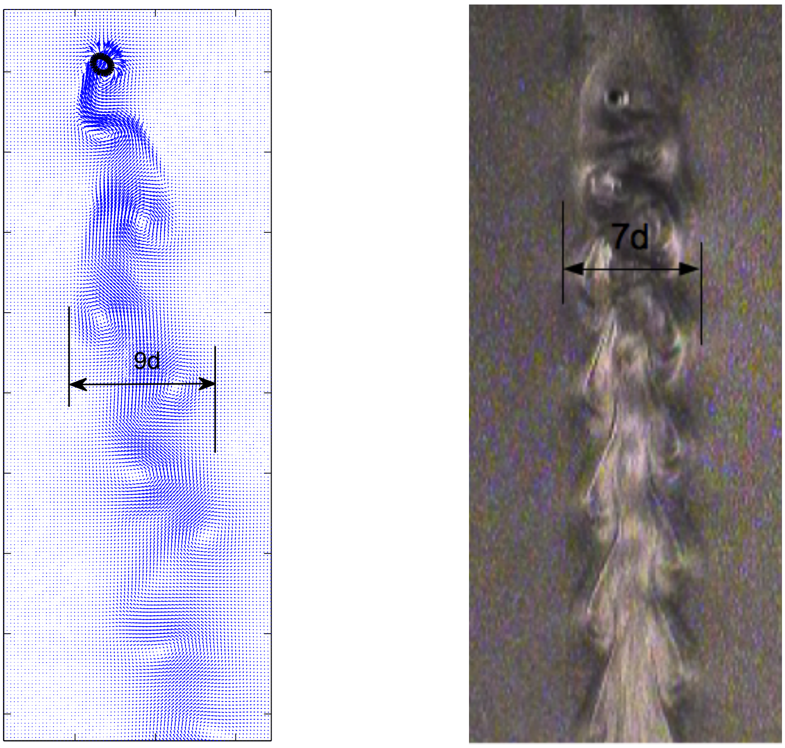

Figure 3.23: Vortex shedding in the wake of the bubble.

3.5 Simulations of multiple bubbles

3.5.1 Overview

As it was mentioned in the opening chapters of this Thesis, the goal of the numerical simulations of bubbles at small scales is to find the information about the behavior of bubbles that the average and engineering models requires for the closure relationships. When a single bubble is simulated very interesting features about the flow generated can be studied and understood, but in real problems the bubble-bubble interaction is very important to understand in behavior of bubbly flows; particularly, to find closures for averaged models. Following this idea, numerical simulations were performed to explore the interaction of multiple bubbles as they ascend. Obviously, the interaction between bubbles is a highly complex phenomenon, and it is impossible to cover it within the present project, Here we only present a sample calculation to demonstrate the modeling capabilities of the numerical tool presently available.

We consider the dynamics of two and several bubbles. The initial conditions for the analysis of two bubbles, are such that the bubbles are placed near the bottom of the integration area, vertically aligned and at a small distance from each other. The initial conditions for the simulation of four bubbles are shown in Figure 3.24. The interaction of bubbles depends strongly on the initial position. Broadly speaking, for large initial distances, the bubble interaction is very weak, since the low pressure patches at the center of the vortices that the preceding bubble generates, dissipate before the trailing bubble interacts with them. However, when the initial distance is small, the second bubble meets strong enough low pressure zones and the interaction occurs, mostly by reducing the drag force and accelerating the second bubble.

An important limitation of the model implemented in this work is that coalescence phenomena are not considered, and then, if two bubbles are close enough to coalesce, the model is not able to remesh completely the bubbles and the front between them disappears. Even when the bubbles move like a single one, numerical errors are present in the interface that should disappear when the coalescence of the bubbles takes place and the merging is not faithfully modeled. For this reason, our numerical simulations are limited to moderate initial distances where coalescence phenomena do not usually appear. The minimum distance for our numerical simulations is about 5 bubble diameters.

The study of multiple bubbles is presented in two parts. In the first part, the motion and interactions of two bubbles are analyzed. We consider that study as the basis for understanding of more complex systems, bubble clouds for example. In the second part, a sample study of the dynamics of several (four, five and six) bubbles is presented. In this case, the dynamics involved is far from being completely understood and requires a great effort to clarify even fundamental issues.

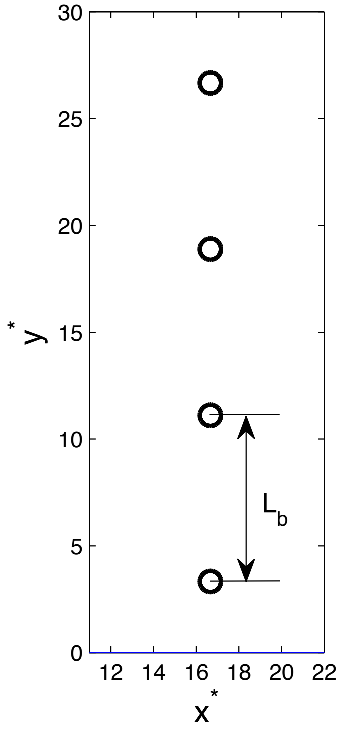

Figure 3.24: Initial conditions for the simulations of multiple bubbles, the distance of the bubbles is L_b and this can vary in order to study the dependence of the interaction of the bubbles over L_b.

3.5.2 Dynamical interaction of two bubbles

The interactions of two bubbles are fundamental to the understanding of the collective motion of a large number of bubbles. When a pair of bubbles are ascending in a viscous fluid at high Reynolds numbers, they tend to interact with each other in an extremely complex way. In this section, some aspects of this phenomenon will be analyzed. Particularly, we describe the zones of strong interaction. In previous sections, the vortex shedding caused by the instability of the wake of a single bubble was described. However, if another bubble moves behind, the vortices shed by the first perturb the otherwise uniform pressure field that second bubble meets, changing its natural trajectory.

Limited information on the interaction of bubbles is available in the literature. Analytical predictions are restricted to very low Reynolds numbers where Stokes flow results show that two bubbles can not change their orientation unless influenced by a third bubble and potential flow models for high Reynolds numbers that indicate that the bubbles oriented in tandem repel each other but bubbles oriented horizontally attract each other. Also, two-dimensional studies have examined the interaction of two bubbles, computations of (Krishna & van Baten 1999) and (Unverdi & Tryggvason 1992). Experimentally observed interactions have been reported as well, (Watanabe & Sanada 2006). It has been concluded experimentally and numerically that a pair of bubbles rising always collided when the Reynolds number is low; however, the authors experimentally observed the existence of an equilibrium distance between a pair of bubbles rising in a vertical line at intermediate Reynolds numbers. On the other hand (Brucker 1999) studied the flow in the wake of single and two interacting air bubbles freely rising in water in a zig-zag path, experiments with two simultaneous released bubbles show that once the second bubble is captured in the wake of the first bubble, it accelerates and rises having a kind of jumps until they collide, and the bubbles coalesce or repel.

The simulations reported in this section were done using the same non dimensional parameters as those of the experiments in the Hele-Shaw cell, i.e. $Ar = 78401$, $Eo = 0.54$ and $M = 2.5 \times 10^{-11}$. As it was described in section 3.2, a single bubble moving at a high Reynolds number, follows a zig-zag trajectory. Now, when two bubbles rise at a high Reynolds number their individual motion can be mostly described in analogous terms, but the occasional interaction of bubbles will perturb the original trajectory of the trailing bubble.

In Figure 3.25, the trajectories of two bubbles (lines red and blue), are shown for different initial distances (5.5, 6.5 and 8 diameters). As it can be observed, in all three cases, the first bubble follows an approximate periodic path similar to an individual bubble (see Figure 3.7), but the trajectory of the second bubble is clearly affected by the wake of the first. As discussed in the previous section, the first bubble sheds alternative vortices with low pressure zones at their centers. These structures are not fixed in space and dissipate due to viscous effects. If the path of the second bubble passes near a strong enough high vorticity, low pressure region, its path will be altered.

In Figure 3.26, the pressure and vorticity fields are shown at the moment when the very strong interaction occurs and the second bubble changes its path. See marker $\circ$ in the central panel of Figure 3.25. In this particular event, the interaction is complex, with the second bubble first turning around the low pressure zone of the vortex, and then ascending again due to the ever present buoyancy force. This situation can be regarded as fresh initial conditions for the rest of the ascending path. It is interesting to observe that in the left and central panels of Figure 3.25, the trajectories of the two bubbles display approximately the same phase, while in the last case, the two paths are dephased.

The flow generated by the first bubble affects the rising velocity of the second bubble, and for this reason the trajectory of the second bubble changes its natural path. The rising velocity alterations can be observed in Figure 3.27, where the bubble velocities in horizontal and vertical directions are shown. The horizontal velocity of the second bubble follows a quasi periodic behavior with some jumps when this bubble finds high vorticity zones, however, around 40 seconds of simulation a large perturbation in the velocity is presented and the behavior of this velocity changes considerably for few seconds. After

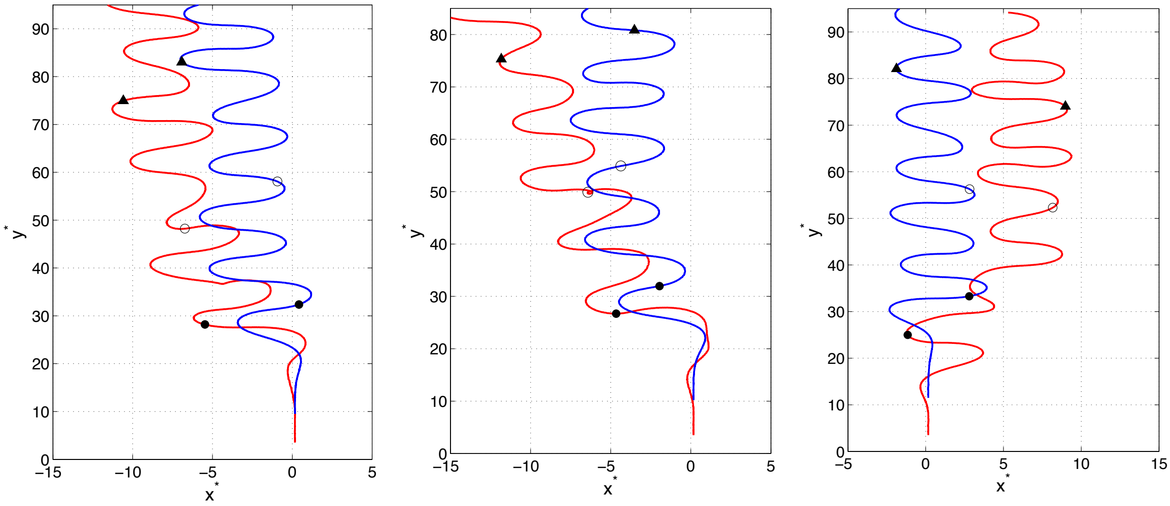

Figure 3.25: Trajectories of the centroid of the two bubbles for initial distances of 5.5, 6.5 and 8 diameters ($Eo = 0.54$ and $Ar = 78401$) are shown in the left, central and right panels respectively. Markers indicate position of bubbles at fixed times.

this jerk, the horizontal velocity takes the quasi periodic behavior again and the bubble rises following a zig-zag motion like a single bubble.

The vertical velocity of the trailing bubble must be analyzed in the same way, but a more interesting feature appears. There are four zones where the vertical velocity is negative, meaning that the bubble descends at some time intervals. The explanation of this phenomena in a buoyancy flow is that the force generated by the pressure of a vortex detached by the first bubble be comparable with the buoyancy force. Then, if the second bubble moves into the vortex region generated by the first bubble, the vortex can force the bubble to turn around it until the vorticity dissipates and the buoyancy force pushes the drop upwards. In some cases, a bubble can turn a complete loop around the vortex. This situation is illustrated with the marker ○ in the central panel of Figure 3.25; this event corresponds to the second zone in which the vertical velocity is negative at 40 seconds of simulation.

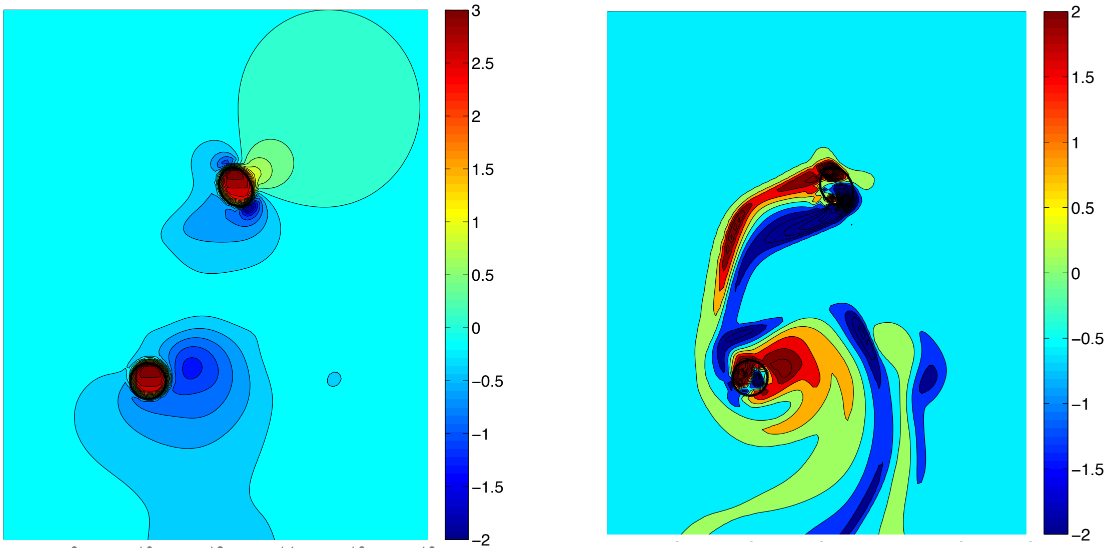

Figure 3.26: Left panel, pressure field and right panel, vorticity field around the bubbles. Initial distance 6.5 diameters. These snapshots correspond to marker ○ in the central panel of Figure 3.25.

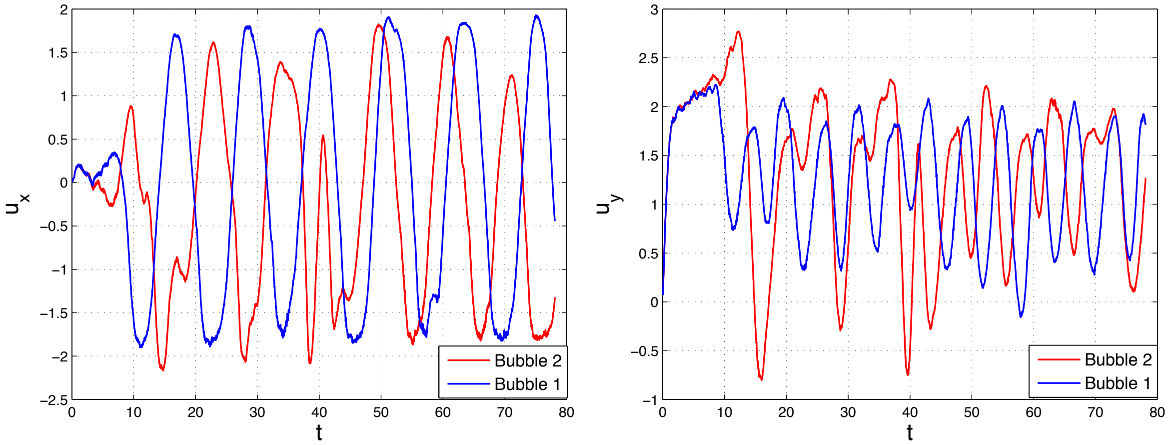

Figure 3.27: Reynolds numbers based on the centroids of the bubbles.

3.5.3 Interaction of multiple bubbles

The last part of this chapter is devoted to the numerical simulations of multiple bubbles. In Figure 3.28, the trajectories of the ascending bubbles are plotted for simulations of four, five and six bubbles, the initial position of the bubbles is shown in Figure 3.24. The dynamics involved and the bubble interactions are very complex. The vortex shedding caused by the instability in the wakes of the bubbles disturbed the trajectories of the following bubbles, with some bubbles accelerating and decelerating. It would be very laborious to interpret in a detailed way the interactions of all bubbles since most of them are coupled.

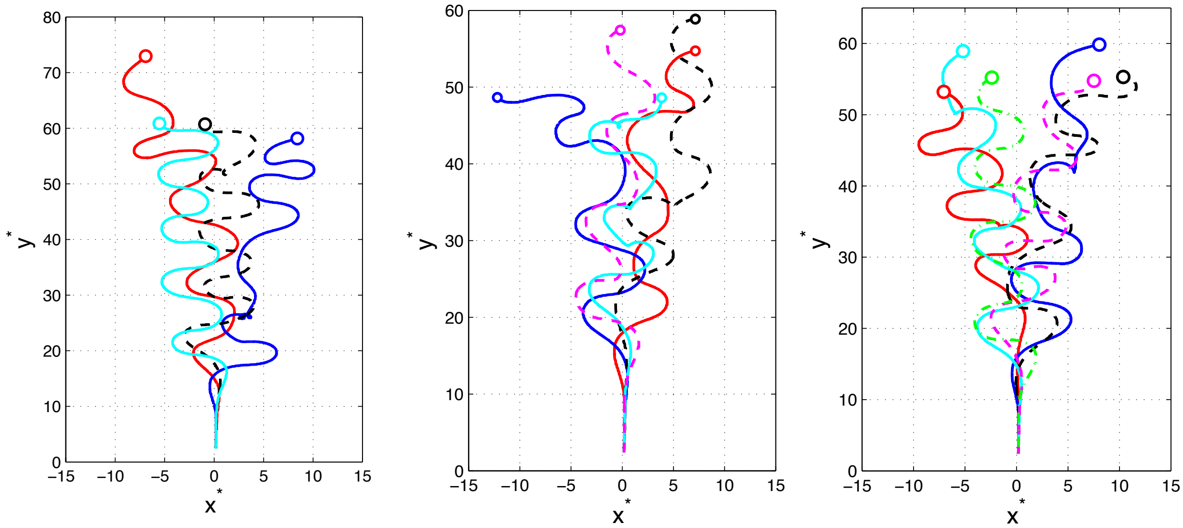

Figure 3.28: Trajectories of the centroid of 4,5 and 6 bubbles for the initial distance of 7 diameters ($Eo = 0.54$ and $Ar = 78401$) are shown in the left, central and right panels respectively.

In a cursory description, it can be said that two different strong interactions can be found in the simulations of multiple bubbles. The first is when a bubble finds a vortex generated by a preceeding bubble and its path changes completely its horizontal motion. This results because the vortex with which the bubble interacts has an opposite motion of the bubble, and the inertial force of such vortex is greater than the the inertial force experienced by the bubble. The second interaction occurs when a bubble is boosted by a vortex detached by another bubble, and it is accelerated. Its trajectory follows the same horizontal motion but with a larger velocity. However, sometimes, the bubble is not only accelerated but is also pulled to the center of the vortex. In this cases the bubble turns around the vortex until the vorticity dissipates and it can follow its natural buoyancy motion. An example of this interaction was commented in the previous section where the motion of two bubbles was analyzed.

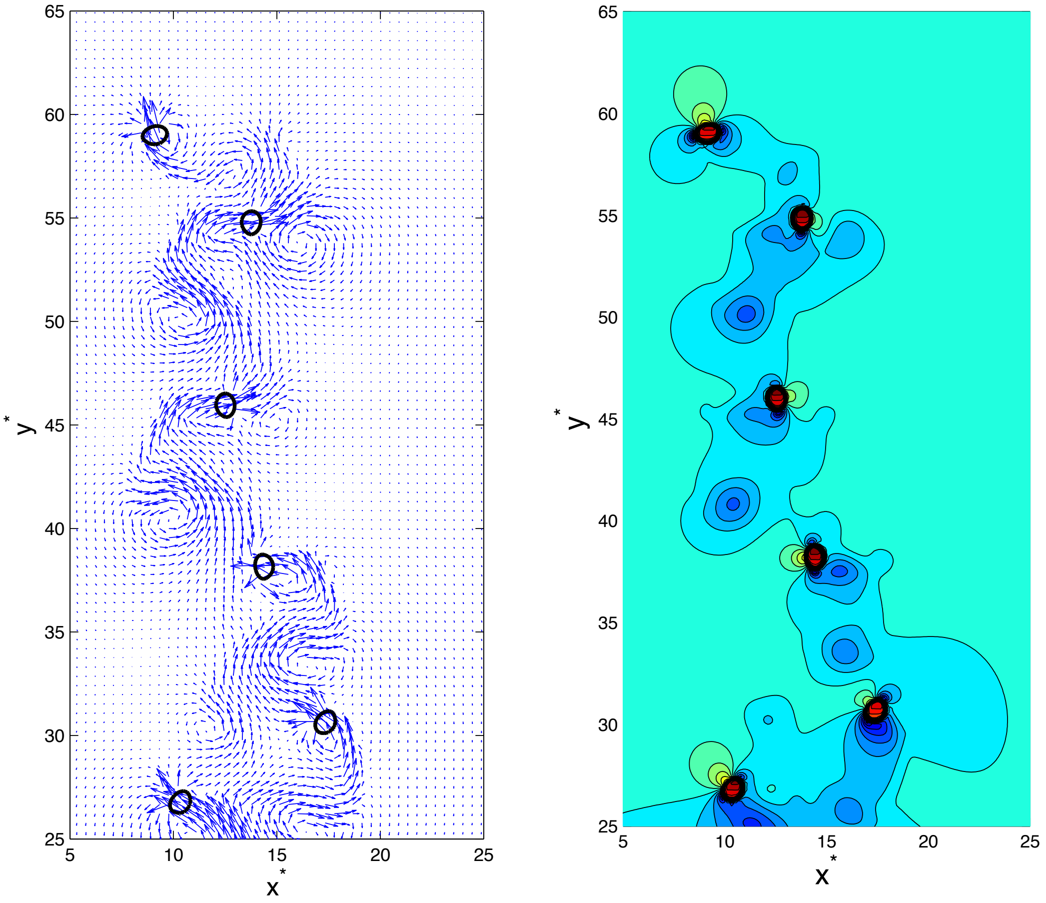

Figure 3.29: Snapshots of the velocity and pressure fields for the numerical simulation of six bubbles rising in a column array (right panel of Figure 3.28).

In Figure 3.29 the velocity and pressure fields are plotted. In the velocity field it can be appreciated that as in the case of a single bubble at high Reynolds number, the instability in the wake of the bubble causes a vortex shedding and a oscillatory motion of the bubble, but in this case the vortices generated in the wake of a bubble are disturbed and occasionally the vortices join to form a stronger vortex. In the pressure field, it is very interesting to note that the bubbles are always linked by a low pressure region created by the transit of the first bubble and intensified by the other bubbles following the same trajectory. Remarkably, bubbles have been observed that do not follow the low pressure path. This phenomenon occurs if the bubble finds a strong vortex that dramatically alters its trajectory with a similar interaction to that described in section 3.5.2.

Conclusions

In this Thesis, the numerical study of the bubble dynamics rising in a column of fluid has been presented. The numerical strategy followed to solve the conservation equations for two immiscible fluids is based on the immersed boundary methods, particularly on the front-tracking method.

The bubble dynamics was studied for a wide range of flow conditions, first the analysis of a single bubble rising at low and moderate Reynolds number was reported. At such flow conditions it was found that the bubbles follows a straight path when it is ascending in the fluid, and that the shape of the bubble depends strongly on the Eotvos number. When the Eotvos number is small, the bubbles present a quasi spherical shape, but for large Eotvos numbers when the surface tension force is small with respect to the viscous forces, the bubbles deform and in extreme cases even a skirted shape is found. At these flow conditions the wake of the bubble is stable and axisymmetric, a dipole is formed around the bubble extending as the bubble is deformed.

The numerical study of a rising single bubble with a high Reynolds number is also described. We found that the dynamics of this phenomenon is very different from what happens at a low Reynolds number. After an initial transient, the trajectory of the bubble centroid describes an approximately periodic zig zag motion, and the bubble acquires an ellipsoidal shape with an inclination that oscillates between ±45°. The flow pattern around individual bubbles is closely related to the von Kármán vortex street. The oscillation of the two open wake recirculation rings from one side of the bubble lower part to the other induces the zigzag path. The vortex shedding the bubbly flows can be used to enhance the mixing processes and also to improve the heat transfer. The comparison of the results obtained from the numerical simulations with experiments in a Hele-Shaw cell, indicate that the trajectory and vertical velocity are in qualitative agreement with the experiments, as is the inclination of the bubble as a function of time.

A simplified model based in that presented by (Pesavento & Wang Jane 2004) was adapted to predict the motion of individual bubbles. The results obtained with this phenomenological model were in agreement with the numerical simulations, and since the model is built in such a way that the total force is split into the forces that have been traditionally interpreted as drag, buoyancy, lift and mass added, the individual effect of those forces could be studied. The buoyancy force pushes the bubble upwards while it was found that the lift force acts as a brake on the vertical motion of the bubble and the vertical mass added force counteracts the vertical lift force.

In the numerical simulations of pairs of bubbles discussed in the section 3.5, we analyzed, somewhat in detail the bubble-bubble interaction through the fluid in the high vorticity, low pressure zones generated by of the wake of the first bubble. We assumed that initially the bubbles are in a vertical arrangement with one bubble leaving at small distance above the other. We found that their interaction is highly dependent on the initial distance. In order to illustrate this effect, we presented the centroid trajectories for three slightly different initial vertical distances. The simulations show that after the initial transient the second bubble follows a similar zig-zag path of the first, but if a vortex behind the first bubble has a high enough vorticity and has low enough pressure, it will be able to critically modify the motion of the second bubble. The simulations of multiple bubbles were done to understand some features of the dynamical interactions in this systems, but the detailed study of the dynamics of the systems when multiple bubbles are involved is a complex problem, and not surprisingly, these systems are not completely understood at this moment. A large number of studies are required to find the precise mechanisms that cause the different trajectories of the bubbles. For the case of the interactions it is necessary to determine the criterium for the bubbles to approach a vortex without a major effect on its trajectory. This kind of studies can be done with the numerical tools from the mathematical model using implementations similar to the model described in this thesis.

There are many unsolved problems on the dynamics of rising of bubbles. However, the numerical tools as the one developed in this work, can be used to better understand the phenomena. The advancement in this field requires new experimental and numerical developments that can address the complexity of these flows and lead to deeper physical understanding as well as to relevant applications.

Bibliography

Andersen, A., Pesavento, U. & Wang Jane, Z. (2005), 'Unsteady aerodynamics of fluttering and tumbling plates', *J. Fluid Mech.* **541**, 65–90.

Bhaga, D. & Weber, M. (1981), 'Bubbles in viscous liquids: shapes, wakes and velocities', *J. Fluid Mech.* **105**, 61–85.

Brucker, C. (1999), 'Structure and dynamics of the wake of bubbles and its relevance for bubble interaction', *Phys. Fluids* **11**, 1781–1796.

Chen, L., Garimella, S., Reizes, J. & Leonardi, E. (1999), 'The development of a bubble rising in a viscous liquid', *J. Fluid Mech.* **387**, 61–96.

Clift, R., Grace, J. & Weber, M. (1978), *Bubbles, drops and particles*, Academic Press.

De la Cruz, L. (2005), Cómputo Paralelo en la Solución Numérica de las Ecuaciones de Balance en Flujo Turbulento, PhD thesis, Universidad Nacional Autónoma de México, Mexico.

Gunsing, M. (2004), Modelling of bubbly flows using volume of fluid, front tracking and discrete bubble models, PhD thesis, Twente University, The Netherlands.

Hua, J. & Lou, J. (2007), 'Numerical simulation of bubble rising in viscous liquid', *J. Comput. Phys.* **22**, 769–795.

Kelley, E. & Wu, M. (2005), 'Path instabilities of rising air bubbles in a hele-shaw cell', *Phys. Rev. Lett.* **79**, 1265–1268.

Krishna, R. & van Baten, J. (1999), 'Rise characteristic of gas bubbles in a 2d rectangular column: Vof simulations vs experiments', *Int.Comm. Heat Mass Transfer* **26**, 965–974.

M. Griebel, T. D. & Neunhoeffer, T. (1998), *Numerical Simulation in Fluid Dynamics: A practical Introduction*, SIAM.

Mougin, G. & Magnaudet, J. (2002), 'Path instability of a rising bubble', *Phys. Rev. Lett.* **88**, 1.

Ohta, M., Imura, T., Yoshida, Y. & Sussman, M. (2005), 'A computational study of the effect of initial bubble conditions on the motion of a gas bubble rising in viscous liquids', *Intnl J. Multiphase Flow* **31**, 223–237.

Patankar., S. V. (1980), *Numerical Heat Transfer and Fluid Flow*, McGraw Hill.

Pesavento, U. & Wang Jane, Z. (2004), 'Falling paper: Navier-stokes solutions, model of fluid forces, and center of mass elevation', *Phys. Rev. Lett.* **93**, 14.

Peskin, C. (1977), 'Numerical analysis of blood flow in the heart', *J. Comput. Phys.* **25**, 220–252.

Prosperetti, A. & Tryggvason, G. (2007), *Computational Methods for Multiphase Flow*, Cambridge University Press.

Ramos, E., Sanchez, R., Gonzalez, M. & Herrera, J. (2007), 'Dynamics of chains of bubbles in a hele-shaw cell', *60th Annual Meeting of the Divison of Fluid Dynamics* **52**.

Sanada, T., Shirota, M. & Watanabe, M. (2007), 'Bubble wake visualization by using photochromic dye', *Chem. Eng. Sci.* **62**, 7264–7273.

Scardovelli, R. & Zaleski, S. (1999), 'Direct numerical simulation of free-surface and interfacial flow', *Annu. Rev. Fluid Mech.* **31**, 567–603.

Sussman, M., Fatemi, E., Smereka, P. & Osher, S. (1998), 'An improved level-set method for incompressible two-phase flows', *Computers & Fluids* **27**, 663–680.

Sussman, M., Smereka, P. & Osher, S. (1994), 'A level set approach for computing solutions to incompressible two-phase flows', *J. Comput. Phys.* **114**, 146.

Tryggvason, G., Bunner, B., Esmaeeli, A., Juric, D., Al-Rawahi, N., Tauber, W., Han, J., Nas, S. & Jan, Y. (2001), 'A front-tracking method for the computations of multiphase flow', *J. Comput. Phys.* **169**, 708–759.

Unverdi, S. & Tryggvason, G. (1992), 'A front-tracking method for viscous, incompressible, multi-fluid flows', *J. Comput. Phys.* **100**, 25–37.

van Sint Annaland, M., Deen, N. & Kuipers, J. (2005), 'Numerical simulation of gas bubbles behaviour using a three-dimensional volume of fluid method', *Chem. Eng. Sci.* **60**, 2999–3011.

Versteeg, H. & Malalasekera, W. (1995), *An introduction to Computational Fluid Dynamics, The Finite Volume Method*, Prentice Hall.

Wang Jane, Z., Birch, J. & Dickinson, M. (2004), 'Unsteady forces and flows in low reynolds number hovering flight: two-dimensional computations vs robotic wing experiments.', *J. Expl. Biol.* **207**, 449–460.

Watanabe, M. & Sanada, T. (2006), 'In-line motion of a pair of bubbles in a viscous liquid', *JSME International Journal Series B* **49**, 410–418.